THESIS FOR THE DEGREE OF DOCTOR OF PHILOSOPHY IN THERMO AND FLUID MECHANICS

Evaluation and modeling of the flow in a slotted wall wind tunnel

EMIL LJUNGSKOG

Department of Mechanics and Maritime Sciences

Division of Vehicle Engineering and Autonomous Systems

CHALMERS UNIVERSITY OF TECHNOLOGY

Göteborg, Sweden 2019

Evaluation and modeling of the flow in a slotted wall wind tunnel
EMIL LJUNGSKOG
ISBN 978-91-7905-219-5

Doktorsavhandlingar vid Chalmers tekniska högskola
Ny serie nr. 4686
ISSN 0346-718X
Department of Mechanics and Maritime Sciences
Division of Vehicle Engineering and Autonomous Systems
Chalmers University of Technology
SE-412 96 Göteborg
Sweden
Telephone: +46 (0)31-772 1000

Chalmers Reproservice
Göteborg, Sweden 2019

Evaluation and modeling of the flow in a slotted wall wind tunnel
EMIL LJUNGSKOG
Department of Mechanics and Maritime Sciences
Division of Vehicle Engineering and Autonomous Systems
Chalmers University of Technology

Abstract

As vehicle manufacturers strive to shorten the development time of new models, an increasing share of the aerodynamic development work is shifted from wind tunnel testing of prototype vehicles to numerical simulations of virtual models. However, comparing measurements from the wind tunnel with numerical simulation data is not straightforward due to several interference effects occurring between the wind tunnel and the tested vehicle.

The objective of this thesis is to improve the understanding of the properties of a slotted wall wind tunnel used for automotive aerodynamic testing and enhance numerical simulation accuracy by providing validation between the simulations and physical wind tunnel measurements. This is done by investigating the empty test section flow, as well as both local and global interactions between the wind tunnel and the test object.

Using standard instrumentation that was calibrated in-situ to achieve low measurement uncertainty, it is shown that a swirling flow angularity pattern seen already during the wind tunnel commissioning is still present in the test section. By ruling out two alternative hypotheses on the cause of this pattern, it is concluded that it most likely originates from the fan. It is also demonstrated that the measured levels of flow angularity are unlikely to have a significant impact on the forces measured on a vehicle.

Scale-resolving numerical simulations of the flow in the empty wind tunnel show good agreement with the measured longitudinal pressure distribution in the downstream region of the test section but deviate upstream of the turntable. This is attributed to shortcomings in the modeling of the distributed suction system used to limit boundary layer growth on the floor upstream of the car.

Investigations of the tangential blowing system used to fill in the boundary layer behind the belts in the moving ground system show that the blowers effectively reduce the displacement thickness of the boundary layer as intended and that this can be well represented in numerical simulations using a simplified representation of the blowers. It is also shown that the force differences measured between different configurations of a vehicle can be significantly affected by the tangential blowing.

Simulations of vehicles as tested inside the wind tunnel test section are shown to improve the prediction quality compared to open road simulations. This requires that the process of non-dimensionalizing the forces and pressures are done in the same way for the in-tunnel simulations as in the physical wind tunnel. Furthermore, lift predictions are significantly improved when including the lift acting on the wheel drive unit belts used to rotate the wheels of the test object.

Keywords: Wind tunnel, Ground simulation, Tangential blowing, CFD simulations, Slotted walls, Flow uniformity, Uncertainty quantification

What's next?

ACKNOWLEDGEMENTS

First of all, I would like to thank my supervisor Professor Simone Sebben for giving me the opportunity to pursue a PhD and for supporting me throughout this project. I would also like to thank Professor Lennart Löfdahl, without whom the Road Vehicle Aerodynamics research group would not have existed.

I thank Alexander Broniewicz at Volvo Cars for all the support and for always believing in me, in all matters ranging from planning and conducting wind tunnel tests to choosing restaurants when traveling.

A project like this would never happen without funding, which was provided by Vinnova FFI (Fordonsstrategisk Forskning och Innovation) and Volvo Cars. Computational resources were provided by Volvo Cars, the Swedish National Infrastructure for Computing (SNIC), and the Chalmers Centre for Computational Science and Engineering (C3SE). For this, I am very grateful.

The wind tunnel crew at Volvo Cars has always been very supportive of whatever crazy things I want to do to their tunnel. A special thank you goes to Anders Lindroos for helping me figure out what can and cannot be done in the tunnel, and for having answers to almost all of my at times very strange questions.

To my colleagues, past and present, at the division of Vehicle Engineering and Autonomous Systems: Thank you for the incredibly fun and inspiring work environment. A special thanks to former colleagues Dr. Sabine Bonitz and Dr. Teddy Hobeika, and current coworkers Adam Brandt, Randi Franzke, Pär Pettersson, Sina Torabi, Johannes Törnell and Magnus Urquhart for all the laughs and good discussions of both open- and closed-door nature.

Finally, I would like to thank my friends and family for the support throughout this endeavor, and a special thanks to Malin for making the last two years the best ones yet.

NOMENCLATURE

α	Flow pitch angle	[°]
β	Flow yaw angle	[°]
γ	Ratio of specific heats	[−]
δ	Boundary layer thickness	[m]
δ^*	Displacement thickness	[m]
Δt	Time step	[s]
ρ	Air density	$\left[\mathrm{kg/m^3}\right]$
σ	Standard deviation	
C_D	Drag coefficient	[−]
C_L	Lift coefficient	[−]
C_LF	Front lift coefficient	[−]
C_LR	Rear lift coefficient	[−]
C_P	Pressure coefficient	[−]
P_s	Static pressure	[Pa]
P_t	Total pressure	[Pa]
q	Dynamic pressure	[Pa]
u	Local flow velocity	[m/s]
u_∞	Freestream velocity	[m/s]
$u(x)$	Standard uncertainty of quantity x (1 standard deviation)	
y^+	Dimensionless wall distance	[−]

ABBREVIATIONS

BCD	Bounded Central Differencing
BLCS	Boundary Layer Control System
CFD	Computational Fluid Dynamics
CFL	Courant-Friedrichs-Lewy number
FMR	Flow Measurement Rig
GESS	Ground Effect Simulation System
GUM	JCGM Guide to the Expression of Uncertainty in Measurement
IDDES	Improved Delayed Detached Eddy Simulation
LES	Large Eddy Simulation
MRF	Moving Reference Frame
OAR	Open Area Ratio
PVT	Volvo Cars aerodynamic wind tunnel
RANS	Reynolds Averaged Navier-Stokes
SUV	Sports Utility Vehicle
WDU	Wheel Drive Unit
WLTP	Worldwide harmonized Light vehicles Test Procedure

DEFINITIONS

1 Drag count	$\Delta C_{\mathrm{D}} = 0.001$
1 Lift count	$\Delta C_{\mathrm{L}} = 0.001$

THESIS

This thesis consists of an extended summary and the following appended papers:

Paper A E. Ljungskog, S. Sebben, A. Broniewicz, and C. Landström. "On the Effects of Wind Tunnel Floor Tangential Blowing on the Aerodynamic Forces of Passenger Vehicles". *SAE International Journal of Passenger Cars - Mechanical Systems* 10(2) (2017), pp. 591–599. DOI: `10.4271/2017-01-1518`

Division of work: The wind tunnel tests were planned jointly by all authors, and Ljungskog was responsible for the execution and analysis. The simulations were setup, performed and analyzed by Ljungskog. However, the vehicle simulations were based on a template simulation provided by Landström, and adapted by Ljungskog to include the tangential blowers. The paper was written by Ljungskog and reviewed by the co-authors.

Paper B E. Ljungskog, S. Sebben, and A. Broniewicz. "Uncertainty Quantification of Flow Uniformity Measurements in a Slotted Wall Wind Tunnel". *SAE Technical Paper 2019-01-0656.* Apr. 2, 2019. DOI: `10.4271/2019-01-0656`

Division of work: The Flow Measurement Rig was designed and manufactured by Aiolos Engineering Corporation with input from Ljungskog and representatives of Volvo Cars, including Broniewicz. The measurements were performed by Ljungskog together with an Aiolos representative. The uncertainty quantification was performed by Ljungskog, who also setup, ran and analyzed the CFD simulations as well as wrote the paper. All co-authors provided reviews of the manuscript.

Paper C E. Ljungskog, S. Sebben, and A. Broniewicz. "Flow Angularity Investigations in an Automotive Slotted Wall Wind Tunnel". *Accepted for publication in Energies* (2019)

Division of work: The measurements were planned, performed and analyzed by Ljungskog, who also wrote the paper. The co-authors contributed with discussions, supervision and reviews of the manuscript.

Paper D E. Ljungskog, S. Sebben, and A. Broniewicz. "Inclusion of the Physical Wind Tunnel in Vehicle CFD Simulations for Improved Prediction Quality". *Submitted to Journal of Wind Engineering and Industrial Aerodynamics* (2019)

Division of work: All simulations were setup, performed and analyzed by Ljungskog. The geometry handling and meshing were based on scripts provided by Volvo and rewritten by Ljungskog to include the physical wind tunnel domain. The wind tunnel measurements were designed, performed and analyzed by Ljungskog. Writing of the manuscript was done by Ljungskog, with review and discussions provided by the co-authors.

Other relevant papers:

Paper I	E. Ljungskog, S. Sebben, A. Broniewicz, and C. Landström. “A parametric study on the influence of boundary conditions on the longitudinal pressure gradient in CFD simulations of an automotive wind tunnel”. *Journal of Mechanical Science and Technology* 31.6 (June 1, 2017), pp. 2821–2827. ISSN: 1738-494X, 1976-3824. DOI: `10.1007/s12206-017-0525-2`
Paper II	C. Kounenis, S. Bonitz, E. Ljungskog, D. Sims-Williams, L. Lofdahl, A. Broniewicz, L. Larsson, and S. Sebben. “Investigations of the Rear-End Flow Structures on a Sedan Car”. *SAE Technical Paper 2016-01-1606*. SAE 2016 World Congress and Exhibition. Apr. 5, 2016, pp. 2016–01–1606. DOI: `10.4271/2016-01-1606`
Paper III	M. Urquhart, E. Ljungskog, and S. Sebben. “Surrogate-based optimisation using adaptively scaled Radial Basis Functions”. *Submitted to Applied Soft Computing* (2019)

CONTENTS

Part I

Extended Summary

1 Introduction[1]

Throughout the history of mankind, mobility has been one of the key enablers for exploration. Since the invention of the wheel, ground vehicles in different levels of technological refinement have been used to discover the world. In the society of today, mobility and transportation are perhaps more important to the masses than ever by enabling people to discover the world themselves. Especially the car has long been seen as a symbol for this personal freedom to go almost anywhere and explore, which has likely contributed to its vast popularity.

However, this popularity comes at a cost for the environment. In 2013, 17 % of the global greenhouse emissions originated from ground transportation [9]. This has lead to a push from legislative authorities on the vehicle manufacturers to decrease the CO2 emissions of their vehicles. One way of reducing emissions is to reduce fuel consumption by lowering the aerodynamic drag that the vehicle has to overcome. Hence, a significant part of the development of a new vehicle is spent on optimizing its aerodynamic behavior.

Apart from the legislative demands for reduced emissions, vehicle manufacturers today face increased demands from customers when it comes to such diverse attributes as design, safety, and fuel consumption. This has lead to a situation where a vehicle can be perceived as outdated just a few years after having been released to the market. In order to bring new technology to the market as soon as possible, the time to develop a new vehicle needs to be reduced. As the manufactures strive to achieve such lead-time reductions, new ways of working have to be employed to meet the often very ambitious time reduction goals. One such way of cutting down on both time and cost is to replace some physical testing on prototype vehicles with virtual simulations. In the case of external aerodynamics, this means substituting wind tunnel testing with Computational Fluid Dynamics (CFD) simulations. However, virtual models have to be thoroughly validated before they can replace physical testing.

The most straightforward way of validating a CFD simulation of the aerodynamic performance of a vehicle is to compare it to measurements from a wind tunnel. However, many possible error sources complicate such a comparison. Except for potential shortcomings of the numerical method itself, there are also issues arising regarding the geometric representation of the test object. Furthermore, CFD simulations are typically performed by placing the vehicle inside a very large box-like “virtual wind tunnel”, the layout of which differs significantly from the physical wind tunnel. Hence, no interference effects between the wind tunnel and the test object are taken into account, meaning that a proper validation of the computational method itself cannot be performed unless these interference effects are fully understood or the wind tunnel geometry is included in the simulations. Increased knowledge of the interference effects also allows for a better understanding of how the aerodynamic impact from different configurations evaluated in the wind tunnel compare to real-world conditions, as effects introduced by the wind tunnel interference could be better separated from the actual behavior caused by the vehicle itself.

---

[1] Large parts of this chapter have been carried over from the Licentiate thesis [8]

The need to understand the wind tunnel interference is further accentuated by recent changes in the regulations for the fuel consumption certification of new vehicles. This new set of rules, known as the Worldwide harmonized Light vehicles Test Procedure (WLTP) [10], mandates that not only the fuel consumption for the base variant of a vehicle is measured and reported, but that the effects of optional extras are also taken into account. If all combinations of extras that might influence the aerodynamics of the vehicle were to be tested under the old regulations, hundreds of time-consuming and expensive coast-down tests would need to be performed for each new model. However, WLTP allows for the use of wind tunnel testing instead of coast-down tests if the tunnel fulfills certain criteria, which increases the need for a detailed understanding of how the wind tunnel influences the aerodynamic forces measured on the vehicle.

Furthermore, WLTP states that CFD simulations can substitute some wind tunnel tests if a set of requirements and restrictions are fulfilled, of which validation to wind tunnel data is one. Apart from requiring agreement between forces, the validation also demands that the simulations show similar flow patterns, velocities, and pressures when compared to the wind tunnel. Inclusion of the wind tunnel into the simulation procedure is likely necessary in order to fulfill such requirements, further emphasizing the need to understand the interference effects.

1.1 Objectives and limitations

This work aims at increasing the understanding of the properties of slotted wall wind tunnels in automotive aerodynamics and improving numerical simulation accuracy by providing validation between CFD and wind tunnel measurements. Furthermore, a goal is to lay a foundation for investigating the possibilities to base the requirements used during the vehicle development on virtual methods, as well as using such methods for certification purposes. In order to achieve this, the aim is to improve the understanding of the relationship between results from numerical simulations, physical wind tunnel measurements, and on-road driving.

The work described in this thesis seeks to meet these goals by considering both the flow in the empty test section of the wind tunnel under consideration, and the interaction between test objects and the tunnel. The empty test section flow is investigated mainly using experimental techniques, the data from which are used when improving the numerical simulation methods. For the interaction studies, both local effects from the moving ground system and global interference effects from the geometrical layout of the test section are investigated. This is done using both experimental and numerical methods.

When dealing with interactions between the wind tunnel and the test object, it is natural to consider different correction methods to correct measurement data for interference effects such as blockage and horizontal buoyancy. However, it was decided that investigations of such methods would not be part of the present work.

It was also decided that on-road driving conditions would only be considered using numerical simulations, as physical coast-down tests would significantly increase the scope of the project. Furthermore, the numerical open road simulations would only consider idealized conditions, thereby excluding any influence from surrounding traffic, weather, wind, or any other outside influence besides driving through still air.

1.2 Outline

The next part of the thesis concerns with some theory and background on automotive wind tunnels in general, and the slotted wall wind tunnel of primary interest in this work in particular. This is followed by descriptions of the experimental and numerical methods used in the investigations of the empty test section flow, the boundary interference studies, and studies of the effects of simulating vehicles inside the wind tunnel test section.

Following the description of the methods, the results of the investigations are presented and discussed, beginning with the test section flow studies concerning the longitudinal pressure gradient and the flow angularity. After this, the results of the examination of the interactions between a test object and the wind tunnel are given and discussed, followed by the predictive quality of simulations with a vehicle inside the wind tunnel test section.

The thesis ends with some conclusions and an outlook on possible further work, followed by the appended papers.

2 Automotive wind tunnels[1]

Ever since Frank H. Wenham and John Browning designed and operated the first wind tunnel in 1871 [11, 12], wind tunnels have been integral tools for investigating the aerodynamic properties of different objects. Although the primary use case for the early tunnels was aircraft development, road vehicles have been tested in wind tunnels since at least 1914, when Peugeot performed tests of a racing car in Gustave Eiffel's wind tunnel in Paris [13]. While the first tests were performed in tunnels designed for aeronautic purposes, wind tunnels aimed at automobile testing started to emerge in the 1930s. In the coming decades, many automotive wind tunnels were built, accommodating both model- and full-scale vehicles. However, with some exceptions, almost all testing was performed with a static ground plane until the early 21st century. Despite the increase in computing power and improved fidelity of numerical simulations, a large number of full-scale automotive wind tunnels have been built or upgraded since the turn of the millennium [14–22], indicating that the wind tunnel is still a valuable tool for vehicle aerodynamicists.

The remainder of this chapter gives a brief introduction to the field of automotive wind tunnels, starting with a discussion of boundary interference and the idea of building interference-free wind tunnels. This is followed by a short description of flow conditioning techniques, an overview of how the ground is simulated in wind tunnels, and a description of the wind tunnel under consideration in this work. The chapter ends with a view into the literature on numerical simulations of wind tunnels.

2.1 Boundary interference

The condition an automotive wind tunnel tries to simulate is the car driving on a flat plane in still air, meaning that the flow is only constrained by the flat plane, i.e., the ground. Since the test section boundaries constrain the flow in a wind tunnel test section, the flow conditions will not be the same as for the idealized case the tunnel is set to simulate. The effect of such constraints is called boundary interference and can be divided into separate effects that are commonly assumed to be additive. Two of the important boundary interference effects for automotive tunnels are the so-called solid blockage and horizontal buoyancy, briefly discussed below for open jet and closed wall test sections. For a more in-depth discussion, see for example Cooper [23], Barlow et al. [24], or Pankhurst and Holder [25].

Solid blockage In a closed wall test section, the introduction of a blockage will cause an increase of the streamwise velocity in order for continuity to be fulfilled. This is because the walls do not allow for the streamlines to expand as they would in free air, as shown in Figure 2.1, which would lead to a higher velocity around the test object and thus a higher measured drag.

---

[1] Large parts of this chapter have been carried over from the Licentiate thesis [8]

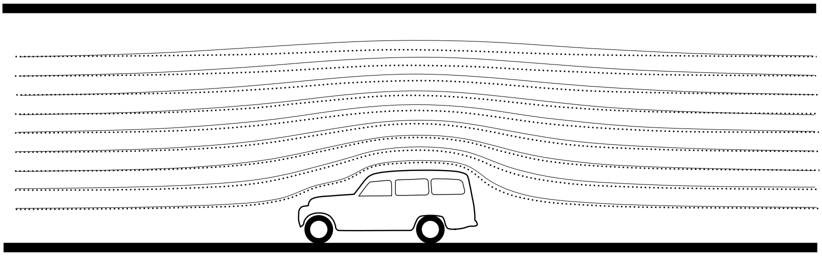

Figure 2.1: *Streamlines for open road (solid) and closed test section (dotted).*

For an open jet test section, the boundary condition of the jet is that of pressure equal to the plenum pressure, which is higher than the static pressure at the corresponding position in the infinite jet encountered in open road conditions. This causes the streamlines to overexpand, resulting in a decrease of the streamwise velocity in the vicinity of the test object and thus a lower measured drag.

Horizontal buoyancy Due to boundary layer buildup on the walls along the length of a closed wall test section, the inviscid core of the flow must accelerate slightly for the stream to fulfill continuity, leading to a decrease in pressure according to Bernoulli's principle. This axial pressure gradient will act as buoyancy in the streamwise direction and will increase the measured drag.

In the open jet case, the axial pressure gradient is not mainly driven by the boundary layer buildup, but rather by the interaction with the nozzle and the collector. Typically, the pressure drops after the nozzle and rises before entering the collector [23]. This interaction can be avoided by placing the test object at a sufficient distance from both the nozzle and the collector. However, this is usually not possible since the usable length of an open test section is limited by the shear layer instability of the jet, meaning that the test object is typically located in a region influenced by either the nozzle or the collector.

2.1.1 Self-correcting wind tunnels

Considering the boundary interference effects described above, it can be noted that the sign of each effect can vary between the two different test section types, and for the horizontal buoyancy in an open jet even within the same test section. Therefore, it might be possible to build wind tunnels that are "self-correcting", for which the boundary interference effects cancel each other out. Two such approaches are briefly discussed here, namely slotted walls and self-correcting open jet type of test sections.

Slotted walls

Slotted walls are not commonly seen in automotive wind tunnels today. The concept originates from the aerospace industry, where large slotted wall wind tunnels have been used since 1949 [26]. A slotted wall test section has walls that are not solid but have longitudinal openings into a plenum. The idea of the slotted walls is to decrease the strong boundary interference experienced in solid wall tunnels by allowing for the jet to expand through the slots when a blockage is introduced into the test section. This approach preserves the long usable length of a closed wall test section that would be limited by strong shear layer instabilities in an open jet.

In the early days of the design of automotive slotted wall tunnels, there was a belief that the slotted wall design would allow for almost interference-free testing [26–29], meaning that self-correcting wind tunnels would be feasible. However, Eng [30] showed that correction is necessary and proposed a method based on closed test section corrections.

Self-correcting open jet

In 1996, Mercker and Wiedemann [31] noted that interference correction for open jet tunnels could not be fully described by the previously known correction methods, and introduced a new method. This approach laid the foundation for the theory of self-correcting open jet wind tunnels, as described by Wickern [32]. The core of his approach is to balance the solid blockage contributions from the nozzle and the overexpansion of the jet by placing the test object closer or further from the nozzle, together with careful design of the collector. The approach of balancing the blockage contributions has some similarities to the slotted wall principle as Wickern [32] notes, in that the behavior of an open jet wind tunnel approaches that of a closed wall test section as the test object is placed closer to the nozzle.

2.2 Flow quality and conditioning

As previously noted, automotive wind tunnels are typically required to simulate the rather idealized conditions of spatially and temporally uniform flow throughout the test domain. This requirement is an inheritance from the time when aerodynamic testing of road vehicles was done in wind tunnels built for the needs of the aeronautical industry. Later on, when specialized automotive wind tunnels were designed and built, the uniformity requirement was carried over [33], possibly as a way of simplifying comparisons between data from different facilities.

However, the on-road wind environment that a vehicle encounters under typical driving conditions is neither uniform in space nor time. These non-uniformities might be caused by a variety of reasons, such as changes in vehicle speed, unsteady wakes of other vehicles, turbulence in the natural wind, or the interaction with road-side obstacles [34]. Thus, in recent years, some automotive tunnels have been upgraded with systems for the generation of turbulence representative of on-road driving [35–39]. These systems have been either implemented as wake generators upstream of the contraction as at Pininfarina [35] and NRC [36] or as movable "flapping" airfoils at the nozzle exit as at Durham University [37], FKFS [38], and Toyota [39].

As stated in Chapter 1, all tunnels used for emissions certification tests under the WLTP regulations [10] need to fulfill certain criteria, of which some are related to flow uniformity. This, together with the fact that fully uniform flow is still the standard test conditions, means that wind tunnels should still be designed for uniform test section flow. In order to achieve such conditions, measures need to be taken during design and construction. Barlow et al. [24], as well as Pankhurst and Holder [25], list some points to address in order to condition the flow and avoiding unwanted non-uniformities. For example, all corners should be equipped with turning vanes to guide the flow adequately and suppress separations. This has the added benefit of reducing the power needed to run the tunnel, thus also reducing the operating costs. Furthermore, swirl from the fan should be reduced by flow straighteners, and care should be taken to avoid separated flow from the fan nacelle. The final flow conditioning is typically done in the settling chamber, where honeycomb structures are used to remove residual swirl or other angularity, and turbulence screens break up larger turbulent structures. Finally, care should be taken to design the contraction such that the wall boundary layer stays attached throughout the length of the nozzle, or severe non-uniformities might occur in the test section.

2.3 Ground simulation

As noted above, the condition an automotive wind tunnel is supposed to simulate is the car driving on an open road in still air. However, in the wind tunnel, the car is stationary and the air moves, meaning that the ground should move with the air to simulate the correct relative motion between the car and the road. The importance of providing the effect of this motion has been well described in the literature, for example by Wiedemann [40, 41]. One study of the effects of proper ground simulation that stands out is the one by Larsson et al. [42], who compared tests for a production car in a wind tunnel without a moving ground to experiments of the same car in a water-filled towing tank that allowed for a correct relative motion between the car and the ground at a representative Reynolds number. They showed that while drag was similar between the two test methods, likely because the drag decrease from the floor boundary layer in the wind tunnel was countered by a drag increase caused by the stationary wheels, the front lift could be as much as 50 % higher in the tunnel. Furthermore, they showed that force differences due to changes on the upper body of the car were well predicted by the wind tunnel but that it failed at predicting differences caused by changes on the underbody.

Achieving an entirely correct ground simulation is in principle possible by using a conveyor belt upon which the car is positioned. Unfortunately, this is impractical for full-scale testing, since the car would need to be held in place by some external structure, which complicates force measurements significantly. This has lead to several techniques being developed to simulate the interaction between the car and the ground. The three most common techniques, namely moving belts, distributed suction, and tangential blowing, will be discussed here. It shall be noted that of the three, only the moving belts provide the correct kinematic boundary condition for the ground, while the two others aim at generating the correct ground interaction by means of boundary layer thickness reduction. However, in most modern wind tunnels, all three methods are used in conjunction in order to exploit their strengths while mitigating their weaknesses.

2.3.1 Moving belts

The possibility of using a moving belt for ground simulation is believed to be introduced already by Gustave Eiffel [33] and was realized by Klemin [43] in 1934. Given that the oncoming boundary layer is completely removed upstream of the belt, the velocity profile at the model location is the same as on the road if using a full-width moving belt. However, the single belt approach is problematic, especially for full-scale testing. Consequently, moving belts were not widely used until the last two decades, when many new wind tunnels were built, and existing tunnels upgraded with a moving ground system [14, 16–19, 21, 22, 44]. Typical for most of these tunnels is that they employ some variant of a so-called five-belt system, which consists of a long center belt running in between the wheels under the car, and four separate wheel drive units that provide the wheel rotation. The car is typically held in place by four struts attached to the jacking points and connected to the underfloor balance. Some facilities even provide two different belt configurations; a five-belt system for passenger vehicle testing and a single- [21] or three belt system [22] for race car testing.

Some of the possible belt configurations that can be used were investigated numerically by Hennig et al. [45]. They found that especially for racing cars with low ground clearance, the improved ground simulation provided by a single- or three belt system is necessary for accurate lift prediction. Furthermore, they concluded that the improved aerodynamic simulation capabilities have to be weighed against the increased technical complexity of the few-belt systems compared to the five-belt variant. This increase in complexity mainly stems from the fact that lift measurements have to be taken through the belt for the single- and three belt configurations since a connection of the whole belts to the balance would lead to large parasitic forces due to the non-uniform pressure field induced by the car on the belt.

2.3.2 Distributed suction

A common approach to prohibit boundary layer growth on a surface is to use distributed suction, as illustrated in Figure 2.2. For an automotive wind tunnel, this is usually done by having a porous plate as the ground and applying suction through the plate, thus removing the low-momentum fluid close to the ground.

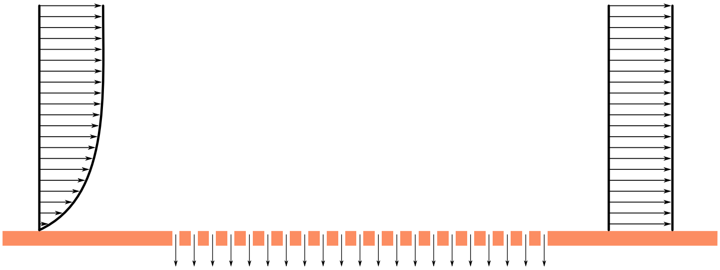

Figure 2.2: *Schematic illustration of distributed suction removing a boundary layer.*

Despite its conceptual simplicity, distributed suction is associated with some difficulties. As noted by Hucho [33], the determination of the correct suction rate is problematic. The suction rate is usually determined for an empty test section, for which it is adjusted to achieve a set displacement thickness at a given location. However, when a test object is introduced into the test section, the flow field changes substantially near the object, thus invalidating the conditions for which the suction rate was calibrated. Furthermore, the test object imposes a pressure distribution on the suction zone, which might change the distribution of the mass flow through the plate.

Apart from the calibration difficulties, Mercker and Wiedemann [46] showed that since it removes mass and momentum from the flow, distributed suction is unable to provide correct boundary conditions underneath a car. They also showed that it could cause significant flow angularity if suction is applied excessively. Wickern et al. [47] further showed that such excessive suction could have a significant impact on the longitudinal pressure gradient in the test section and by that change the measured drag. Due to these concerns, a typical usage of distributed suction is to remove the incoming boundary layer upstream of a moving belt system and downstream of a scoop removing the incoming boundary layer from the nozzle.

2.3.3 Tangential blowing

Another possibility to reduce the influence from the floor boundary layer is to fill in its momentum deficit by injecting a high-speed jet parallel to the ground, which is the basic principle of tangential blowing, as illustrated in Figure 2.3.

One major shortcoming of tangential blowing is that the desired displacement thickness can only be obtained for one specific streamwise location. However, Mercker and Knape [48] showed that good agreement to moving ground measurements could be attained for drag by choosing this location as the location of the front wheels, even though this lead to an overprediction of lift.

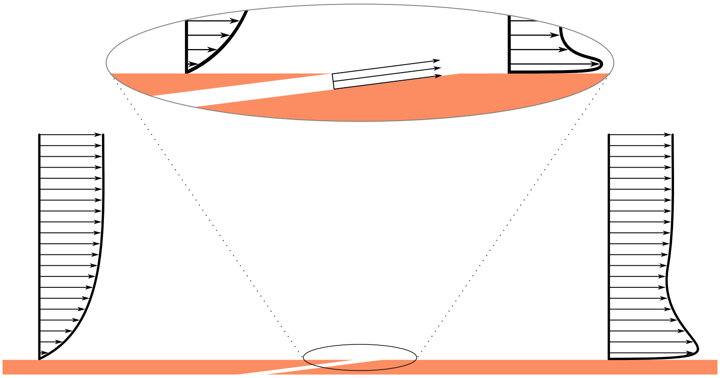

Figure 2.3: *Schematic illustration of a tangential blower filling in the momentum deficit in a boundary layer.*

Mercker and Wiedemann [46] concluded that tangential blowing has some advantages over distributed suction, despite its shortcomings. For example, the imposed flow angularity is significantly smaller than for suction, and the adverse effect of momentum removal seen from suction is avoided.

In modern installations, tangential blowing is often used in conjunction with moving belts and distributed suction. A typical use case is to fill in the boundary layer created on the strip of stationary ground often found downstream of a distributed suction zone and upstream of a moving belt. Another use case is to mount the blowers just downstream of a belt to extend the apparent length of the belt.

2.4 The Volvo Cars aerodynamic wind tunnel

The wind tunnel under consideration in this thesis is the Volvo Cars full-scale aerodynamic wind tunnel (PVT). An overview of PVT can be seen in Figure 2.4. The tunnel is located in Gothenburg, Sweden, and is of closed return (Göttingen) type with a slotted wall test section. It is equipped with systems for control of both temperature and humidity, making it capable of both aerodynamic and thermodynamic testing. When running thermodynamic tests, the test object is mounted on a dynamometer, which is located downstream of the turntable and underfloor force balance.

When the tunnel was built and commissioned in the mid-1980s, it was not equipped with a moving ground system. In 2006, it was upgraded with a five belt moving ground system and a 5 MW fan, allowing wind speeds of up to 250 km/h. A description of the upgrade was given by Sternéus et al. [17].

An overview of the technical specifications of the wind tunnel is provided in Table 2.1. Descriptions of the moving ground system, the test section flow quality, and the repeatability of the force measurements are given in the following sections.

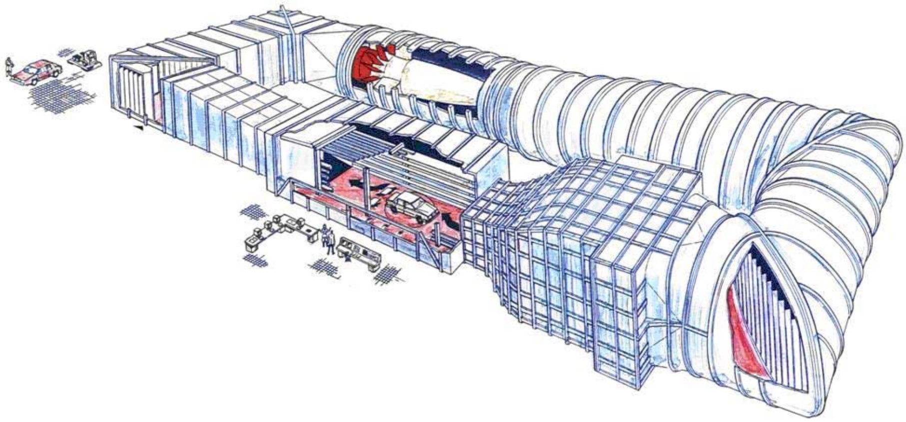

Figure 2.4: *Overview of the Volvo Cars aerodynamic wind tunnel (PVT).*

Table 2.1: Summary of the technical specifications of the Volvo Cars aerodynamic wind tunnel. The flow quality data is taken from the commissioning report [49].

Overall layout	
Type	Closed return (Göttingen)
Contraction ratio	6:1
Fan	5 MW with 9 blades, 8.15 m diameter
Test section	
Type	Slotted Walls
Open area ratio	30 %
Dimensions	6.6 m × 4.1 m × 15.8 m, (W×H×L)
Cross-sectional area	27.06 m^2
Flow	
Maximum wind speed	250 km/h
Wind speed determination	Nozzle method, pressure drop between settling chamber and nozzle outlet
Dynamic pressure uniformity at turntable center	$\sigma = 0.3\,\%$
Flow angle uniformity at turntable center	$\sigma_\alpha = 0.29°$ (Pitch)
	$\sigma_\beta = 0.18°$ (Pitch)
Turbulence level at turntable center	0.1 %
Moving ground system	
Type	Five belts with boundary layer scoop, distributed suction and aft-belt tangential blowing
Boundary layer thickness at turntable center	$\delta^* = 0.35\,\mathrm{mm}$
Velocity range	7 km/h to 260 km/h
Turntable and balance	
Turntable diameter	6.6 m
Yaw angle range	±30°
Angle resolution	±0.05°
Balance	Pfister six component underfloor balance
Thermodynamics	
Temperature range	20 °C to 60 °C
Relative humidity	10 % to 90 %
Solar simulation	816 W/m^2 to 1200 W/m^2 full spectrum
Dynamometer	Located downstream of the turntable, 2WD, absorbing up to 225 kW

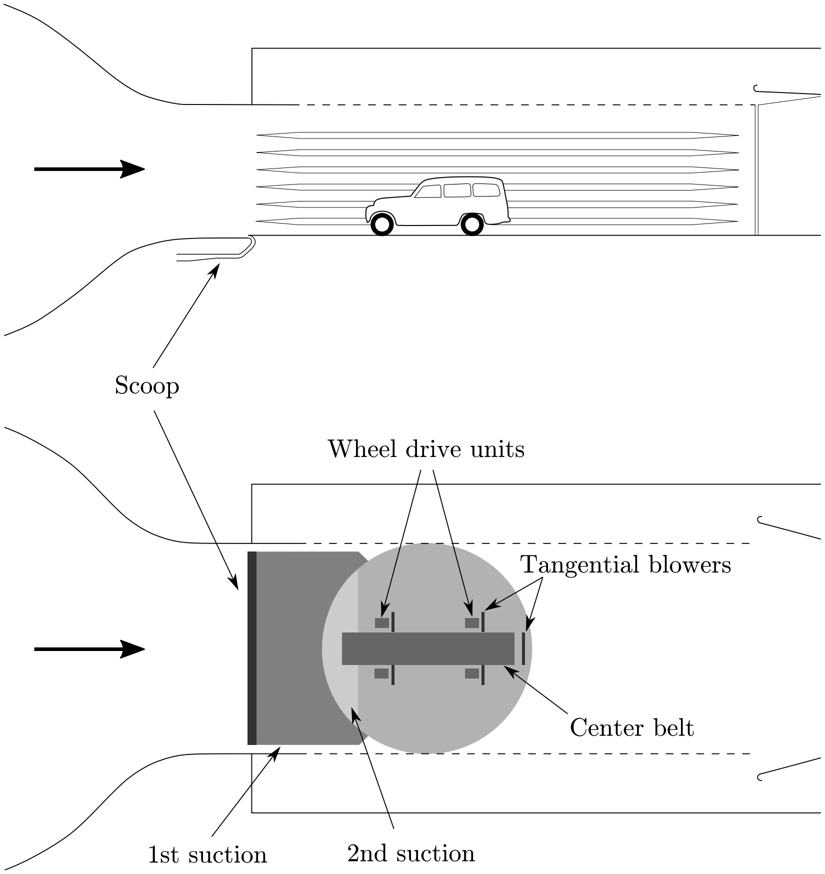

Figure 2.5: *Layout of the boundary layer control system in PVT.*

2.4.1 Boundary layer control and moving ground system

The five-belt moving ground system in PVT is illustrated in Figure 2.5. Beginning at the nozzle outlet, the boundary layer control system starts with a basic suction scoop, driven by a separate 250 kW fan and capable of removing up to 30 $\mathrm{m^3/s}$ of air through its 75 mm tall and 6030 mm wide opening. Its role is to take out the boundary layer buildup from the floor of the nozzle. The air removed by the scoop is reinjected above the slotted roof.

The floor area between the scoop and the turntable consists of a perforated floor, with an open area ratio of 8.9 %, which constitutes the first distributed suction system able to remove up to 7.7 $\mathrm{m^3/s}$. The second distributed suction system is similar to the first, but with smaller holes and an open area ratio of 4.5 %. This subsystem has a removal capacity of 2.05 $\mathrm{m^3/s}$ and is mounted on the upstream part of the turntable. Most of the air removed by the distributed suction systems is injected back into the wind tunnel outside of the slotted walls.

Table 2.2: Permissible wheelbase and track width ranges in PVT.

Property	Min [mm]	Max [mm]
Track width	1380	1657
Wheelbase	2032	3200

A fraction of the air removed by the second distributed suction is reinjected through the tangential blowing system. This system consists of five separate blowers, one mounted downstream of each moving belt. The more typical installation with tangential blowing upstream of the belts was rejected during the upgrade of the wind tunnel as it was deemed to be located too close to the front wing when testing Formula 1 cars [17]. Each blower mounted behind one of the Wheel Drive Units (WDU) consists of a 0.6 mm tall and 600 mm wide slot, from which the air is exiting after passing through a settling chamber under the floor. The center belt blower is of similar construction, but with a 1 mm tall and 1 m wide blowing slot. All five blowers are pressurized by the same compressor and can be individually adjusted either by a valve mounted before each settling chamber or by changing the slot height.

As previously mentioned, the rolling road itself consists of five separate belts. Each belt can be controlled individually and does not have to follow the wind speed. The 0.8 mm thick steel center belt is 1 m wide and 5.3 m long and is suspended on two 590 mm diameter rollers, of which the position of the rear one is continuously corrected by a computer to adjust the tracking of the belt. In between the rollers, the belt is floating on an air lubrication system, consisting of alternating suction and blowing regions through porous graphite. This ensures that the belt does not overheat due to friction, or lifts at low-pressure regions under the test object.

The floor on the turntable can be reconfigured and the four wheel drive units moved to account for different wheelbases and track widths within the ranges given in Table 2.2. The WDU belts can be changed between three different widths; 280, 360 and 420 mm, in order to handle different tire widths. In contrast to the center belt, the wheel drive units are connected to the underfloor balance. Furthermore, load cells between each WDU and the balance frame allow for measurement of the tractive force needed to rotate each wheel to within ±2 N. The same air lubrication method used for the center belt is also used for the WDU belts.

While mounted on the turntable, the test object is held in place by four struts connected to the balance and the vehicle jacking points. These struts can be positioned independently of the wheel drive units to allow for different vehicle types to be tested. The vehicle ride height can be adjusted within the ±50 mm stroke of the struts during a test, and the whole vehicle can be raised 400 mm between runs to enable configuration changes to the underbody. Another type of struts that do not constrain the vehicle movement in the vertical direction is also available. Using these “floating” struts allows for investigations of, for example, lift induced ride height- or attitude changes.

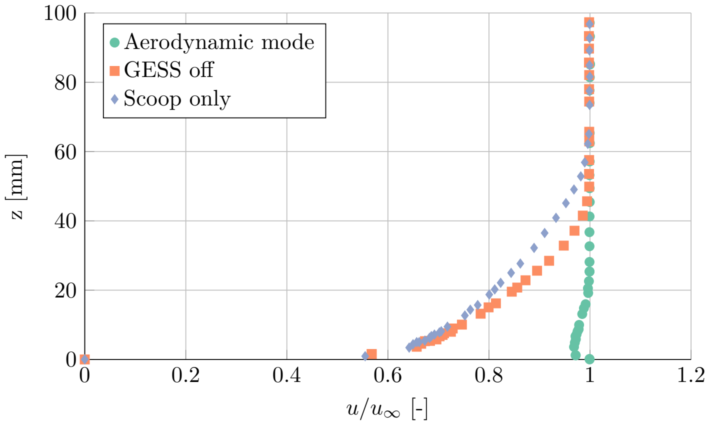

Figure 2.6: *Boundary layer profiles measured at the turntable center at a freestream velocity of* $u_\infty = 200\,\mathrm{km/h}$. *Data from Sternéus et al. [17].*

Boundary layer thickness

The effect of the moving ground system can be seen in Figure 2.6, showing the boundary layer profiles at the turntable center ($x = 0$, $y = 0$). Data are shown for three different operating modes for the moving ground system. In the aerodynamic mode, all systems described above are active, while in the GESS off (Ground Effect Simulation System off) mode, only the basic suction scoop and the two distributed suction systems are active. For the scoop only mode, all systems except for the scoop are turned off.

For the aerodynamic mode, a small velocity deficit can be seen. This is caused by an unavoidable step from the plate upstream of the belt down to the belt [17]. The deficit leads to a relatively large boundary layer thickness of $\delta \approx 16\,\mathrm{mm}$, as shown in Table 2.3. However, since the deficit is rather small, the displacement thickness is only $\delta^* \approx 0.35\,\mathrm{mm}$.

As expected, the boundary layer is considerably thicker for the GESS off and scoop only modes. For the scoop only mode, the upgrade commissioning [49] showed that the boundary layer grows to a thickness of $\delta \approx 20\,\mathrm{mm}$ over the distributed suction zones when they are deactivated, which causes the difference seen at the turntable center in Table 2.3.

Table 2.3: Boundary layer and displacement thickness at the turntable center for the different operating conditions in PVT. Data fromSternéus et al. [17].

Operating condition	δ [mm]	δ^* [mm]
Aerodynamic mode	16	0.35
GESS off	45	7.5
Scoop only	63	10.1

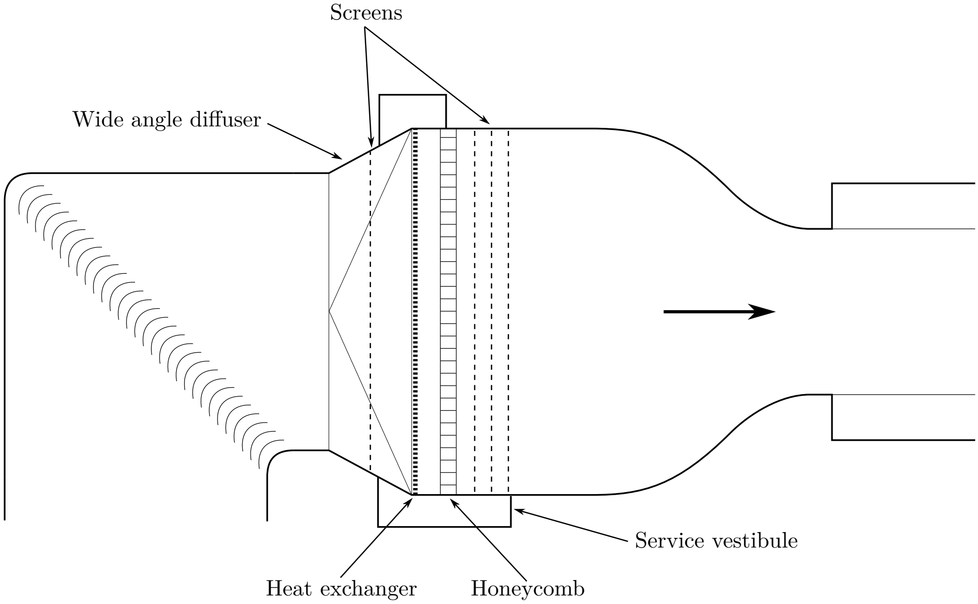

Figure 2.7: *The installation of flow conditioning devices in the settling chamber.*

2.4.2 Flow conditioning and quality

In order to provide good flow quality in the test section, several of the techniques described in Section 2.2 are employed. Each corner has guide vanes helping the flow turn, and a total of four anti-turbulence screens are mounted together with a heat exchanger and a honeycomb structure in the settling chamber upstream of the contraction and nozzle. Since the heat exchanger is a large loss device, it helps to make the flow more uniform before it enters the honeycomb for alignment. Downstream of these two devices, three of the screens act as smaller loss devices to further improve the spatial uniformity of the flow. The flow is then accelerated through the 6:1 contraction. A sketch of the different flow conditioning devices in the settling chamber can be found in Figure 2.7

These flow conditioning measures results in a low turbulence flow in the test section, as low as 0.1 % [50] average over a cross-plane located at the turntable center. Furthermore, the dynamic pressure standard deviation over the same plane is $\sigma < 0.4\,\%$ [17, 50].

The flow angularity measured on the aforementioned plane during the two commissioning campaigns is visualized in Figure 2.8. It can be seen that a vortical structure is present in the flow for both data sets and that the upgrade commissioning data show a larger downwash in the lower center region caused by the distributed suction system. Furthermore, differences can be seen in the upper corners of the test section, where the more recent measurement shows a flow more directed inwards and downwards.

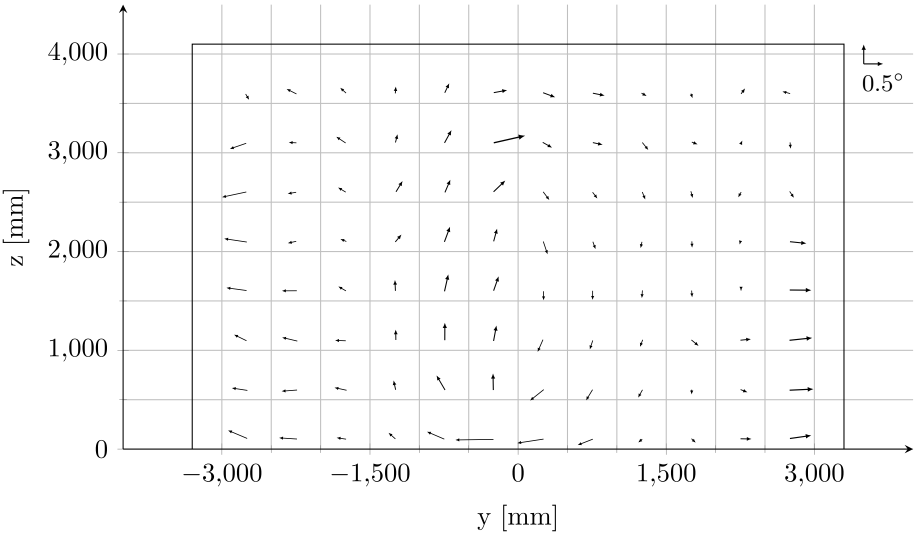

(a) *Original commissioning in 1986, measured at 180 km/h.*

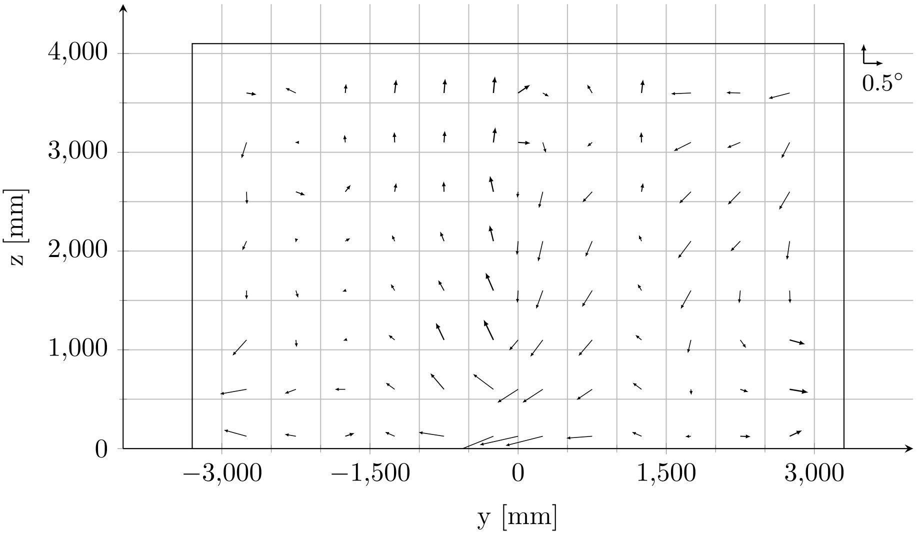

(b) *Upgrade commissioning in 2006, measured at 140 km/h.*

Figure 2.8: *Flow angularity at the turntable center plane as measured during the two commissioning campaigns. Data from the respective commissioning reports [49, 51]. Arrows in upper right corner show the magnitude of* 0.5° *flow angularity in pitch and yaw.*

Table 2.4: Repeatability of force coefficients.

Force	Coefficient	Repeatability	
		Within test	Between tests
Drag	C_D	±0.001	±0.003
Front lift	C_{LF}	±0.001	±0.008
Rear lift	C_{LR}	±0.005	±0.008

2.4.3 Force coefficient repeatability

As for all physical measurements, wind tunnel force measurements are associated with some degree of variability. The variability level in PVT is characterized by the repeatability of the measured force coefficients, given in Table 2.4. Such a characterization can be done in two ways; within a test and between two tests. For the former, the car stays mounted in the test section for all measurements, while for the latter, the car is removed from the test section and reinstalled.

It can be noted that although the front- and rear lift coefficient repeatability is the same between tests, they differ significantly within a test. The reason for this is that the between test repeatability is mostly determined by the installation of the vehicle, which might differ slightly between tests. On the other hand, the within test repeatability is mostly determined by unsteady flow behavior around the car and thereby the averaging time. The front of the vehicle is subjected to a very steady oncoming flow, and hence the front lift is quite steady, whereas the rear lift is more affected by the unsteady flow under the car and in the base wake. The rear lift within test repeatability could thus be reduced by averaging the force measurements over a longer time. However, the current levels have been determined to be a reasonable tradeoff between repeatability and productivity for vehicle development work.

2.4.4 Coordinate system

The coordinate system in PVT is a right-hand oriented system with its origin at the turntable center. Positive z is directed upwards with $z = 0$ at the floor, and positive x is in the streamwise direction. All coordinates throughout the remainder of this thesis are given in this coordinate system.

2.5 Numerical simulation of wind tunnels

As discussed, the improved requirements on simulation accuracy have increased the need for inclusion of wind tunnel effects in numerical simulations during recent years. This has lead to several papers being published on the subject. The usual approach taken for simulation of automotive wind tunnels can be divided into two groups; using the standard box-type CFD simulation domain with the inclusion of the ground simulation system from the physical wind tunnel, or inclusion of the full geometry of the high-speed leg, including contraction, test section, and diffuser.

Many of the simulations of automotive wind tunnels described in the literature have been performed on open jet tunnels [52–56], with some exceptions for closed wall tunnels mainly used for testing of commercial vehicles [57, 58]. A general conclusion is that the simulation accuracy, when compared to physical tests, tends to increase when the wind tunnel geometry is taken into account. For example, Fischer et al. [53] simulated a detailed scale model of a notchback in two different configurations of an open jet wind tunnel and compared the forces to both blockage free CFD simulations and measurements in the physical tunnel. They found that for the one wind tunnel configuration with the larger interference effects, the accuracy of the CFD simulations improved when the wind tunnel geometry was included in the simulations, compared to the blockage free simulations. Furthermore, they noted that some of the differences seen between the physical force measurements and the simulations with included wind tunnel geometry corresponded to a difference between the measured and simulated longitudinal pressure distribution in the empty test section, and concluded that the pressure variations are important to capture in the simulations.

Some studies have also been performed for a slotted wall configuration [59–61]. The study of Perzon [59] was one of the first published on CFD simulations of wind tunnel interference in automotive aerodynamics. He concluded that the flow field of the simplified vehicle considered changes inside of the wind tunnel as compared to blockage free simulations. However, the simulation method used then does not meet modern standards in terms of, for example, mesh resolution or the applied turbulence model, thus making his conclusions uncertain. The more recent investigations of the same wind tunnel by Olander [60] and Wall [61] showed some discrepancies between the simulated and measured flow field in the empty test section. They hypothesized that these differences might have been caused by anomalies upstream of the simulated region, or by uncertainties in the modeling of the moving ground system. They did also not achieve a consistent improvement of the simulation accuracy of forces on vehicles over open road simulations by including the wind tunnel domain, which can likely be attributed to shortcomings of the employed steady-state method and the non-dimensionalization of the forces for the in-tunnel simulations.

3 Methodology

This chapter describes the methods used for the different investigations, which have been divided into three parts; the empty test section, the interaction between the test object and the wind tunnel, and numerical simulation of a test object inside the test section.

3.1 Empty test section investigations

A reasonable first step to improve the understanding of the behavior of a wind tunnel is to measure and simulate the empty test section flow. Hence, extensive experiments, both physical and numerical, investigating global and local flow behavior, have been performed. This section is devoted to descriptions of the different experimental setups used in the empty tunnel, including some uncertainty quantification, as well as a description of the numerical modeling of the test section flow.

3.1.1 Measurement of the longitudinal pressure distribution

To validate numerical simulations of the empty test section flow, the longitudinal static pressure distribution was measured. Furthermore, the WLTP regulations [10] mandate that the pressure difference between two points at half the nozzle height and 3 m up- and downstream of the turntable center should be measured to within

$$|C_p(x = -3\,\mathrm{m}) - C_p(x = 3\,\mathrm{m})| \leq 0.02$$

if vehicle certification measurements are to be performed in the wind tunnel.

The measurements were performed using a Prandtl tube mounted on a custom-built streamlined rig, shown in Figure 3.1. The wing was constructed such that the Prandtl tube was placed in the lateral and vertical center of the test section. It was then moved in the streamwise direction, and measurements were taken at in total 51 points. The reason for measuring at this height instead of closer to the floor was that the WLTP requirement for the longitudinal pressure gradient is set at half the nozzle height.

The differential pressure between the total- and static pressure ports, denoted P_{Prandtl}, was measured using the wind tunnel differential pressure transducer. The pressure coefficient was then computed as

$$C_{\mathrm{P}} = \frac{-P_{\mathrm{Prandtl}} + k_{\mathrm{q}}\Delta P_{\mathrm{nozzle}} + k_{\mathrm{p}}\Delta P_{\mathrm{nozzle}}}{k_{\mathrm{q}}\Delta P_{\mathrm{nozzle}}} - \frac{k_{\mathrm{p}}}{k_{\mathrm{q}}},$$

where $\Delta P_{\mathrm{nozzle}}$ is the pressure drop over the nozzle used to calculate the freestream wind speed, and k_{p} and k_{q} are two calibration coefficients derived during the commissioning of the wind tunnel. The reason for using this method instead of directly measuring the static pressure with the standard pressure measurement system was the better accuracy of the differential transducers.

Figure 3.1: *Prandtl tube mounted on the custom-built wing used for measurements of the longitudinal pressure distribution.*

It can be noted from the figure that the wing was fairly large when considering the short standoff distance of the probe. However, the interference effect is expected to be constant for all measurement positions, and the data were thus offset such that $C_{\mathrm{P}}\,(x = 0) = 0$.

3.1.2 Measurement of tangential blowing uniformity

The uniformity of the boundary layer thickness downstream of the tangential blowers was measured in order to quantify the effectiveness of the boundary layer reduction and to serve as a validation for numerical simulations of the blowers. The measurements were done using a rake of 22 total pressure probes mounted on the wind tunnel traversing gear, as shown in Figure 3.2. The rake was swept across the width of each blower, at a downstream distance of 800 mm from the slot. This position was chosen to correspond with the position for which the tangential blowers were calibrated during commissioning [49].

Tangential blowing systems often result in a velocity overshoot downstream of the blowing slot. Hence, the boundary layer thickness cannot be robustly defined as a percentage of the freestream velocity, since the velocity profile is not monotonically increasing throughout the boundary layer. In order to avoid such problems, the boundary layer thickness was instead quantified using the displacement thickness δ^*, which is more robust to non-monotonic velocity profiles due to it being an integrated quantity, as can be seen from its definition

$$\delta^* = \int_0^\infty \left(1 - \frac{u(z)}{u_\infty}\right) \mathrm{d}z,$$

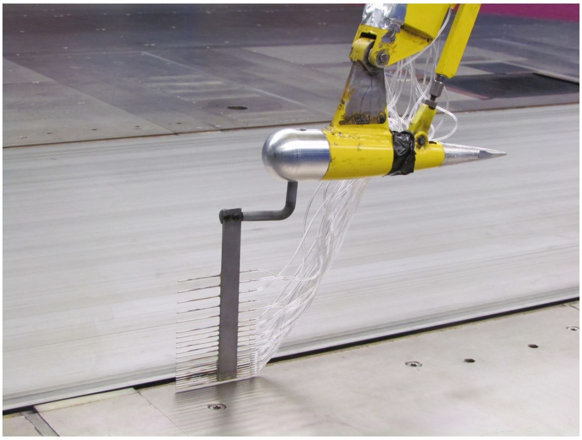

Figure 3.2: *Boundary layer rake mounted on the traversing gear.*

where the local velocity $u(z)$ is calculated as

$$u(z) = \sqrt{\frac{2q(z)}{\rho_{\mathrm{s}}}}.$$

The dynamic pressure $q(z)$ is computed from the total pressure measurements using the compressible flow relation

$$q(z) = \frac{\gamma}{\gamma + 1} P_{\mathrm{s}} \left(\left(\frac{P_{\mathrm{t}}(z) - P_{\mathrm{s}}}{P_{\mathrm{s}}} + 1 \right)^{\frac{\gamma - 1}{\gamma}} - 1 \right),$$

where $\gamma = 1.4$ is the ratio of specific heats for air.

3.1.3 Flow uniformity measurements

As a means to understand the test section flow and to provide data for validation of numerical simulations, the flow uniformity in terms of flow angularity and static pressure was measured in the test section. This also served as a health-check of the tunnel as no such measurements had been performed since the moving ground upgrade. During the commissioning campaigns after the tunnel construction in 1986 and the upgrade 20 years later, such measurements were performed using the so-called commissioning strut shown in Figure 3.3. This strut consisted of a vertical strut with a traversing unit able to move the single probe assembly in the vertical direction. The strut was hanging from a roof-beam screwed to the roof and attached to the floor by a floor-beam. Both these were made of steel and allowed for the strut to be repositioned at 13 predetermined lateral positions. To move the assembly in the longitudinal direction, everything had to be disassembled and reassembled at the new position. Due to the heavy parts and the fact that mounting the roof-beam required scaffolding to be brought into the test section, the installation was hazardous, laborious, and slow. Furthermore, the single probe and

Table 3.1: Requirements on test section flow uniformity that the new rig should be able to demonstrate.

Flow variable	Requirement
Static pressure	$\sigma(C_{\mathrm{P,s}}) < 0.4\,\%$
Total pressure	$\sigma(C_{\mathrm{P,t}}) < 0.15\,\%$
Flow angularity	$\sigma(\alpha)$, $\sigma(\beta) < 0.15°$
Turbulence	$T_{\mathrm{ux}} < 0.1\,\%$

slow traversal speed resulted in low measurement productivity, thus disqualifying the commissioning strut as a viable alternative for extensive measurements that had to be accommodated in the regular testing schedule of the wind tunnel.

The Flow Measurement Rig

Due to the shortcomings of the existing commissioning strut, a new rig for flow uniformity measurements was acquired. The operational requirements set for the new rig stated that installation, extensive testing, and full removal from the test section should be possible with only two available working shifts of six hours each. Furthermore, it should be possible for two wind tunnel technicians to perform the installation, operation, and removal, while no residual parts should be left to influence the flow in the test section outside of periods of usage. For the measurement quality, it was decided that the accuracy of the measurements should be good enough to demonstrate flow quality within the bounds given in Table 3.1, where $\sigma(x)$ denotes the standard deviation of flow quantity x over a cross-plane in the test section.

The new Flow Measurement Rig (FMR) can be seen in Figure 3.4. In contrast to the commissioning strut, the new rig has eight probes in fixed positions and does not need a roof-beam for support. Instead, it is held in place by two floor-beams, upon which it can be moved laterally in 13 predetermined positions by sliding on a linear rail on the rear beam and low-friction plastic on the front. It is also significantly lighter, since the strut, its supports, and the probe arms are made of carbon fiber with aluminum inserts in the joints. The material choices allowed for a slender structure while keeping sufficient stiffness, which, together with the longer standoff distance of the probe arms, resulted in smaller rig-induced interference effects compared to the old strut.

Each of the eight probe arms was designed to accommodate 5-hole AirData probes for simultaneous measurement of static pressure, total pressure, and flow angularity. They can also be equipped with hotwire probes for turbulence surveys. In order to facilitate the flow angularity calibration procedure described below, each probe arm is fastened to the vertical strut with a clevis bracket allowing for the pitch angle of the arm to be adjusted. Furthermore, the probe supports at the end of the arms allow for the probe to be rolled in precise 90° steps.

Figure 3.3: *The old commissioning strut mounted at the upstream end of the test section.*

Figure 3.4: *The new Flow Measurement Rig (FMR) mounted at the turntable center.*

Probe calibration

In order to fulfill the set requirements, the individual probes had to be calibrated for static pressure and flow angularity. All calibrations were performed in-situ in the test section at three velocities, 100, 140 and 200 km/h.

Static pressure correction Since the eight individual probes might yield slightly different pressure readings, the data need to be offset to a common reference. If absolute pressure readings were of interest, this would mean a full calibration in a known flow. However, since the purpose of the FMR is to measure the uniformity of the flow, it is sufficient to use one of the probes as the reference.

The individual probe corrections were found by measuring the total and static pressure in turn for each probe in the same position. The procedure showed that the probe-to-probe variations in total pressure were negligible, why only the static pressure was corrected. This was done by normalizing the measured pressures and computing the correction for probe i in reference to probe 1 as

$$\Delta C_{\mathrm{p},i} = C_{\mathrm{p},i} - C_{\mathrm{p},1}.$$

This value was then used to correct the static pressure measurement for probe i as

$$C_{\mathrm{p},i,\mathrm{corrected}} = C_{\mathrm{p},i,\mathrm{measured}} - \Delta C_{\mathrm{p},i},$$

which yielded results independent of the variations between the probes, but with all probes deviating from the true C_p by the same amount as probe 1.

Flow angularity calibration For the accuracy of the flow angularity measurements to fulfill the set requirements, the probes had to be calibrated in situ. The calibration method follows the procedure described in the AIAA Recommended Practice on Calibration of Subsonic and Transonic Wind Tunnels [62]. The probes had to be calibrated for both pitch and yaw, but since the procedures are identical save the difference that the probes being rolled 90° for the yaw calibration, only the procedure for calibrating the pitch angles is given here.

For sufficiently small flow angles, the measured pressure coefficient difference between two opposing holes on the probe can be assumed to be linear in the flow angle relative to the flow tip. Denoting this pressure coefficient difference ΔC_P and the probe-relative flow angle α_m, this relation can be written as

$$\Delta C_\mathrm{P} = M\alpha_\mathrm{m}, \tag{3.1}$$

where M is the probe sensitivity. However, the sought-after flow angle is the one relative to the test section centerline, and not relative to the probe. From the definition in Figure 3.5, it can be seen that

$$\alpha_\mathrm{m} = \alpha_0 + \alpha_\mathrm{p} + \alpha_\mathrm{f}, \tag{3.2}$$

where α_0 is the probe offset relative to the probe arm, α_p is the angle of the probe arm relative to the wind tunnel centerline, and α_f is the sought-after flow angle. Solving for α_f yields

$$\alpha_\mathrm{f} = \frac{\Delta C_\mathrm{P}}{M} - \alpha_0 - \alpha_\mathrm{p},$$

where the sensitivity, M, and the offset to the probe arm, α_0, can be determined from the calibration. The angle of the probe arm, α_p, however, has to be measured. For pitch, this could be done using an inclinometer, which is not possible for yaw. Here, a Trimble S7 total station [63], as shown in Figure 3.6, was used to measure both the pitch and yaw angles of the probe arms. This was done by measuring the spatial position of two reference points on each arm, from which the angles were calculated.

By varying the pitch of the probe arm, α_p, between $-2°$ and $2°$ in $1°$ increments and recording the difference in pressure coefficient between the top and bottom holes on the probe tip, a linear fit can be obtained between the pressure difference and the probe arm angle. Since the objective is to determine two different variables (M and α_0), the procedure needs to be repeated with the probe rotated 180° around its axis. These rotations are denoted as the probe being in its “upright” and “inverted” position, respectively. Performing a linear fit between the measured ΔC_p and α_p in the upright position yields

$$\Delta C_\mathrm{P,up} = m_\mathrm{up}\alpha_\mathrm{p} + b_\mathrm{up}, \tag{3.3}$$

where $m_\mathrm{up} = M$ and $b_\mathrm{up} = M(\alpha_0 + \alpha_\mathrm{f})$, as can be seen by comparison with Equations (3.1) and (3.2). Repeating with the probe inverted yields an expression similar to (3.3), with $m_\mathrm{inv} = -M$ and $b_\mathrm{inv} = M(\alpha_0 - \alpha_\mathrm{f})$, since, in the inverted case,

$$\alpha_\mathrm{m} = -\alpha_0 + \alpha_\mathrm{p} + \alpha_\mathrm{f}.$$

The angular sensitivity M and probe-to-arm offset α_0 can then be written as

$$\begin{cases} M = m_\mathrm{up} = -m_\mathrm{inv} \\ \alpha_0 = \dfrac{b_\mathrm{up} + b_\mathrm{inv}}{2M}. \end{cases}$$

Correction for rig interference

Even though the interference from the new flow measurement rig is smaller than for its predecessor, it should still be corrected for. This is also the case for uniformity measurements since the design of the FMR results in a non-uniform interference at the different probe tips. The corrections for static pressure and flow angularity were determined using a numerical approach, which was validated using static pressure measurements in the physical tunnel.

The numerical simulations followed the procedure described in Section 3.1.5, with some differences. First of all, one simulation with the FMR included in the simulations, as shown in Figure 3.7, was run for each of the 13 possible lateral positions of the rig. This was since the strut interference was expected to interact with the slotted walls. The differences

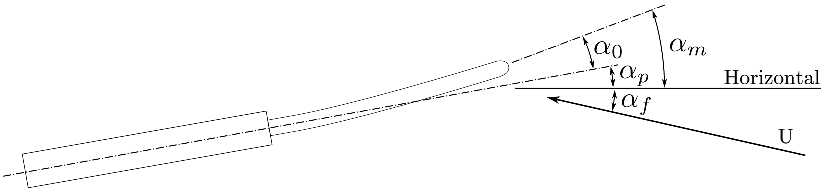

(a) *Upright position*

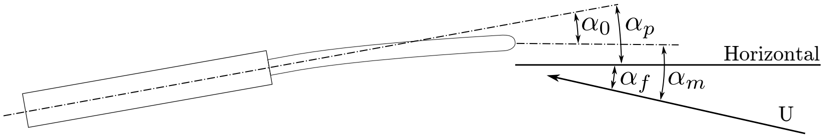

(b) *Inverted position*

Figure 3.5: *The relation between the different probe angles.*

Figure 3.6: *The total station used to measure the angles of the probe arms.*

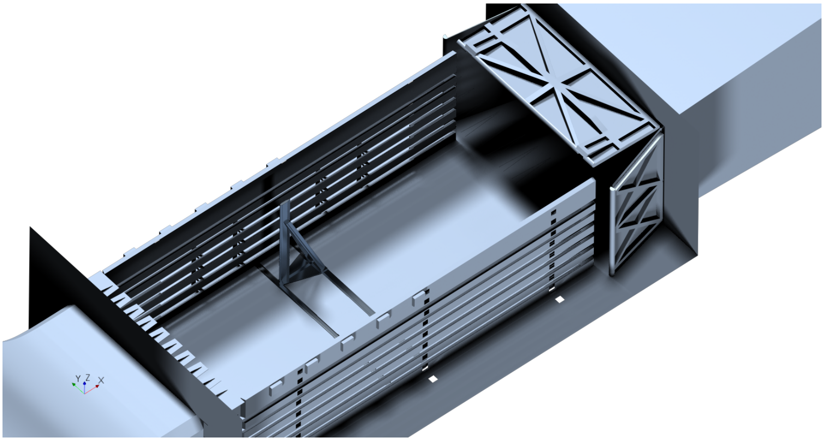

Figure 3.7: *The FMR in the numerical model of the test section. The plenum walls and slotted roof are hidden for visibility.*

in static pressure and flow angularity compared to an empty test section simulation were then computed at each probe position. Furthermore, significant refinements were added around the strut, which, together with 12 prism layers on the FMR to achieve $y^+ < 1$, resulted in a cell count of about 140 million. The sampling time was also increased from 3 s to 10 s to reduce the noise levels since the differences to resolve were expected to be small.

In order to validate the numerical simulations, the static pressure was measured at five longitudinal positions ranging from 600 mm to 2065 mm in front of the leading edge of the FMR using a 1.2 m tall floor-mounted Pitot-static tube and at 3.1 m height using a roof-mounted probe, as shown in Figure 3.8. Since the roof-mount held one of the probe arms usually attached to the FMR itself, the FMR had to be positioned 250 mm off-center to enable measurements at the closest separation distance. However, since the only purpose of the measurements was to validate the numerical simulations in which the FMR can be placed in any position, this was not an issue. To correct for the longitudinal pressure gradient in the empty test section, a second set of measurements were taken at the same axial positions with the FMR removed. These pressures were then subtracted from the original measurements in the same manner as for the simulations.

Investigations of flow angularity causes

As discussed in Section 2.4.2, a vortical flow structure has been observed in the test section since the tunnel was taken into service. The rotational direction of this structure corresponds to that of the fan, and it is thus possible that it is caused by residual swirl from the fan not fully countered by the flow conditioning devices. However, it has been hypothesized that issues in the flow conditioning itself could cause the vortical flow. This hypothesis has been tested by altering two of the conditioning devices.

Figure 3.8: *The interference measurement setup measuring static pressure in front of the FMR at* $z = 1.2\,\mathrm{m}$ *and* $z = 3.1\,\mathrm{m}$.

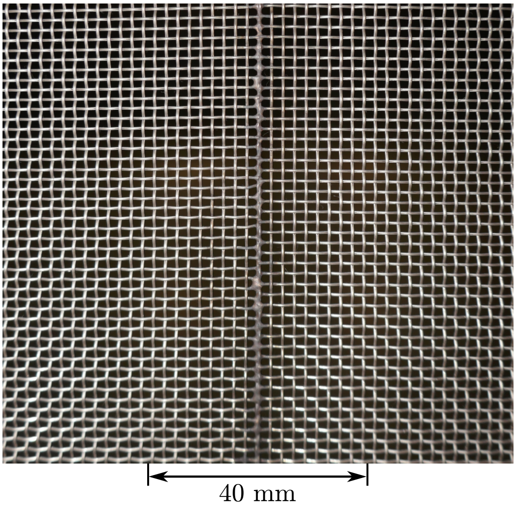

Figure 3.9: *Close-up view of the weld between two screen halves.*

Leakage flow around the heat exchanger core The heat exchanger in the settling chamber, as outlined in Figure 2.7, is mounted such that the heat exchanger core spans the full width and height of the settling chamber. The pipes supplying the core with cooling water are thereby mounted in service vestibules outside of the airstream. These vestibules are sealed towards the atmosphere, but not to the air-path, meaning that air can bypass the core through the vestibules. Furthermore, the slot the air is leaking through ranges between approximately 10 mm to 40 mm along the height of the heat exchanger, which has been proposed being the cause of the vortical flow pattern in the test section. This hypothesis was tested by measuring the flow angularity before and after sealing the leak using tubular pipe insulation and tape.

Impact from the welds in the turbulence screens Another potential cause of flow angularity in the test section is the way the turbulence screens are mounted. Due to the large size of the settling chamber, each of the three downstream screens is made up of two parts that are welded together on the lateral centerline. This weld introduces a small blockage, as shown in Figure 3.9, which lines up for all three screens. The possible impact of this blockage was investigated by measuring the test section flow angularity before and after adding a 40 mm wide tape strip to the upstream side of the most downstream screen, as shown in Figure 3.10. The motivation for exaggerating the influence from the weld in this way was that if no significant effects on the flow angularity could be measured with such a comparatively large disturbance, it could be concluded that the welds themselves are not causing the observed swirling flow pattern.

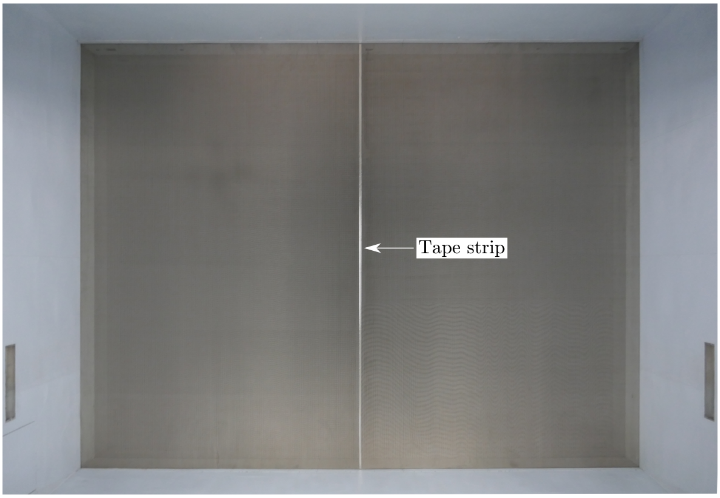

Figure 3.10: *A 40 mm wide tape strip added over the weld of the most downstream screen.*

3.1.4 Quantification of measurement uncertainties

For all the flow quantity measurements, the uncertainties were computed in accordance with the JCGM Guide to the Expression of Uncertainty in Measurement [64] (GUM). The first step of the quantification of the total uncertainty of the flow variables of interest was to quantify the uncertainties of the measured quantities, such as pressures and probe position. These were then propagated through the post-processing of the measurement data using the linear error propagation theory as implemented in the `Measurements.jl` [65] package in the Julia programming language [66]. This allowed for both the computation of the overall uncertainties and the contribution from each measured quantity.

According to the GUM, the uncertainties of the measured quantities can be quantified using two different approaches, called *Type A* and *Type B*. For the former, the variability is established using repeated measurements, while the latter is based on scientific judgment with its basis in other available data such as previous experience, manufacturer's specifications, or calibration data. The GUM further states that the Type A approach is not necessarily more reliable than Type B, mainly since the number of samples is typically low in many Type A settings due to time or budget constraints. For both methods, the variability is expressed as a standard deviation, and no distinction is made between them in later stages of the post-processing.

For the measurements in this work, both Type A and Type B approaches have been used, and the estimated standard uncertainties of the measured quantities can be seen in Table 3.2. For the pressure measurements done during the measurement of the static pressure gradient and the boundary layer thickness, the specified accuracy of the respective pressure transducers were converted to standard deviations in accordance with the GUM. This was done by assuming a rectangular distribution with the width $2a$ corresponding to

Table 3.2: Standard uncertainty components for each of the measurements.

Source of uncertainty	Standard uncertainty	Value
Static pressure distribution		
Differential pressure transducer	$u(p)$	0.58 Pa
Angularity-induced pressure uncertainty	$u(\beta)$	0.29 %
Boundary layer uniformity		
Pressure measurement system	$u(p)$	1.56 Pa
Probe rake position	$u(z)$	5×10^{-4} m
Flow uniformity		
Pressure measurement system	$u(p)$	0.11 Pa
Total station	$u(x)$	6×10^{-4} m
CFD correction for static pressure	$u(C_{\mathrm{p,s}})_{,\mathrm{CFD}}$	0.0005
CFD correction for pitch angle	$u(\alpha)_{,\mathrm{CFD}}$	0.01°
CFD correction for yaw angle	$u(\beta)_{,\mathrm{CFD}}$	0.02°

the width of the span between the accuracy bounds, which yielded the standard deviation

$$\sigma = \frac{a}{\sqrt{3}}.$$

The positional uncertainty of the boundary layer rake used to measure the boundary layer uniformity, and the angular uncertainty of the mounting of the probe used for measuring the longitudinal pressure distribution were estimated in a Type B approach. The angular uncertainty of the Prandtl tube was based on the play in the bracket connecting the wing to the slotted roof and was then converted to a maximum deviation in the measured dynamic pressure of about 0.5 % according to the relation given by Barlow et al. [24].

For the flow uniformity measurements, the uncertainty of the pressure measurements was quantified using a Type A approach with 10 repeated measurements at the same location in the wind tunnel with offset calibrations (tares) performed between each measurement. The reason for not using the specified accuracy, as previously described, was that all the uniformity measurements were always referenced to another simultaneous pressure measurement and were taken within one calibration of the pressure transducer. According to the manufacturer, the main source of uncertainty for the pressure measurement system stems from the calibration of the pressure transducer that is performed at the beginning of each measurement campaign. Thus, the expected uncertainty is smaller when not performing re-calibrations between measurements.

A similar approach was used for the measurements of the probe arm angles performed with the total station. The standard uncertainty was computed based on 10 repeated

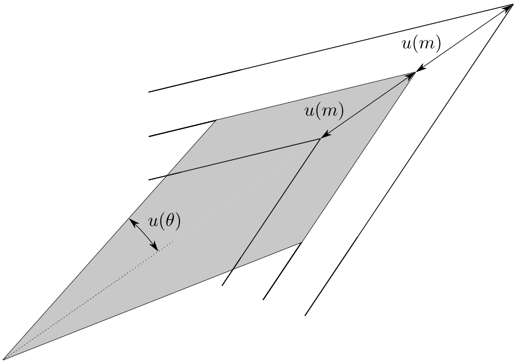

Figure 3.11: *Definition of angular- and magnitude uncertainty in the glyphs proposed by Wittenbrink et al. [67].*

measurements of a point with a known position, with the total station removed from its tripod and repositioned between measurements. Due to time constraints, this could not be done inside the test section, meaning that a different set of reference points used to locate the total station had to be used. These reference points were not placed as accurately as the ones used for the actual measurements in the test section, most likely resulting in a too pessimistic estimate of the measurement uncertainty.

The uncertainty of the CFD simulations used to correct for the interference caused by the rig was estimated using a Type B approach based on previous experience, as well as the correlation with the validation measurements. It should be noted that the given uncertainties are for the correction, i.e., the difference between a simulation with the strut in place and a simulation of the empty test section. It is thus very likely that the uncertainty of the absolute values from the simulations are significantly larger.

Visualization of uncertainty for vector quantities

It is often helpful to indicate the uncertainty of a measured quantity graphically, which for a scalar quantity can be done using error bars. However, this is not as straightforward for a vector field, which has uncertainties associated with both magnitude and direction. In this work, the glyphs introduced by Wittenbrink et al. [67] are used. These glyphs indicate the angular uncertainty $u(\theta)$ by increasing the width of the arrow and the magnitude uncertainty $u(m)$ with two arrow tips, as shown in Figure 3.11.

3.1.5 Numerical simulations of the empty test section

All simulations of the empty test section were performed in STAR-CCM+, and included the full high-speed leg of the wind tunnel, as shown in Figure 3.12. The geometry included the settling chamber, contraction, slotted wall test section, and diffuser, with an added extension between the diffuser and the outlet. The test section contained all the major parts, including wall supports, ventilation ducts, and the return flaps. However, some details, such as cables and auxiliary equipment that are mounted in the plenum outside the slotted walls and roof, were omitted to reduce the geometrical complexity.

The inlet was set as a mass flow inlet, with the mass flow tuned so that the velocity at a point 1.2 m above the turntable center was 140 km/h. This corresponds to the position for which the wind speed is calibrated in the physical tunnel. The outlet aft the extension was set to a pressure outlet condition with zero gauge pressure.

The geometry was meshed with trimmed hexahedral cells and between 1 and 10 prism layers on the walls. The height of the first prism layer was set to 2 mm, and the total prism layer thickness and number of layers were adaptively adjusted to achieve a growth rate of 1.5 between the prism layers and into the core mesh. This resulted in a mesh consisting of approximately 95 million cells and $30 < y^+ < 150$ on the test section walls. The reason for not resolving the boundary layers with $y^+ < 1$ was that all expected separations are well-defined at sharp edges, such as the slot openings, and that the benefit of a well-resolved boundary layer thereby would not overweigh the added computational burden. No formal mesh study was performed. However, some simulations were run on a significantly refined mesh consisting of approximately 180 million cells. These simulations did not yield a difference in the predicted longitudinal pressure gradient, which was used to compare the simulation outcomes.

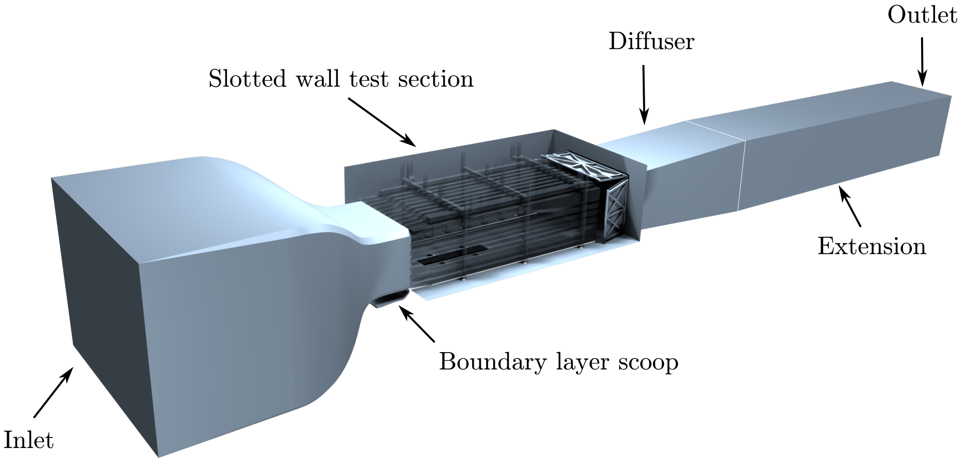

Figure 3.12: *The wind tunnel geometry used in the simulations.*

Turbulence was modeled using the Improved Delayed Detached Eddy Simulation (IDDES) formulation [68] of the SST $k - \omega$ turbulence model with the so-called All y+ wall treatment. The solution was initialized with a steady-state solution and allowed to develop for 2.5 s before averaging the flow fields for 3 s, corresponding to about seven flow passes through the test section. The temporal resolution was 2.5×10^{-4} s, which resulted in CFL numbers below unity in the majority of the domain. A shorter time step of 1×10^{-4} s was also tested but did not result in a significantly different mean flow field compared to the longer time step.

Treatment of the boundary layer control system

Of the different parts of the boundary layer control system described in Section 2.4.1, only the boundary layer scoop had its geometry included in the simulation domain, as shown in Figure 3.12. A mass flow boundary condition was set on the end to extract air from the domain at a specified rate. Due to the infeasible amount of cells needed to resolve the perforated plates in the distributed suction systems, a different approach was taken. The two systems were modeled as patches on the flat floor using the boundary condition introduced by Cyr et al. [55], which acts as a slip wall with a prescribed mass flow in the wall-normal direction. All the air removed by the scoop and the distributed suction systems was re-injected into the domain in the same locations as in the physical tunnel, meaning above the slotted roof for the scoop and outside the slotted side walls for the distributed suction. As in the physical tunnel, a fraction of the air from the second distributed suction system was fed to the five tangential blowers. These were modeled using the approach presented by Olander [60], in which a mass flow inlet condition was set on a patch of the floor, with an injection direction almost parallel to the ground. The five moving belts were modeled with a moving wall condition and ignoring all small gaps around the belts in the physical tunnel.

Validation of the boundary layer control system modeling To validate the modeling of the distributed suction, a section of the perforated suction plate was resolved in a simplified simulation domain shown in Figure 3.13. The boundary conditions, with a velocity inlet at 140 km/h, a pressure outlet at zero gauge pressure, and a mass flow outlet in the cavity under the 0.25 m × 0.5 m section of perforated floor, were set to match the conditions in the full-scale simulations of the physical tunnel. Furthermore, the side walls, top, and floor patches up- and downstream of the suction regions were set to slip walls. The hole size and distribution, as well as the suction mass flow, were chosen to correspond to a patch of the same size of the first distributed suction system in the physical tunnel. In order to resolve the flow in the holes, a mesh consisting of approximately 17 million cells was used, while turbulence was modeled using a steady-state $k - \varepsilon$ RANS model. This simulation was used as the baseline, to which a second simulation using the same general domain and setup, but applying the suction through the same custom boundary condition used in the full-scale simulations, was compared. Using the same refinement levels for the ground in the second simulation as in the full-scale test section simulations resulted in a mesh of approximately 100 000 cells, which illustrates the significant cost increase introduced when resolving the perforated floor.

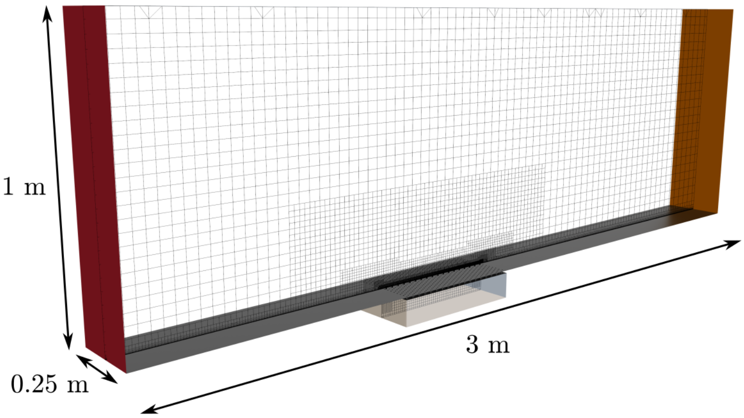

(a) *Overview with the mesh displayed on the domain center plane.*

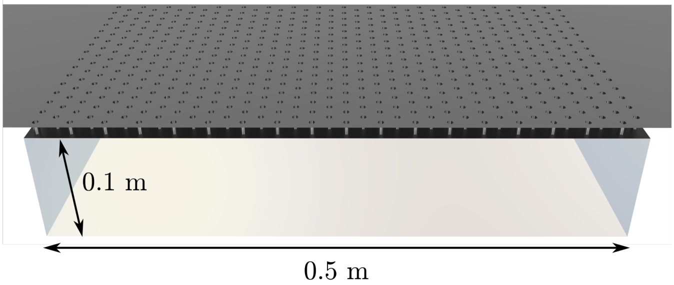

(b) *Perforated plate and cavity.*

Figure 3.13: *The domain used for the validation of the distributed suction modeling.*

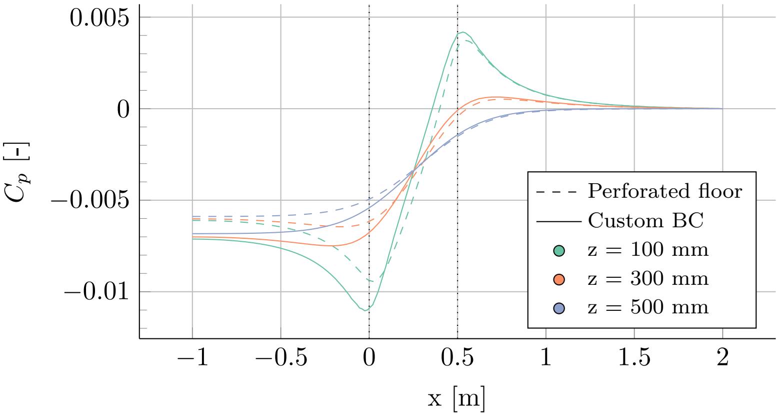

Figure 3.14: *Longitudinal pressure development over two suction zone implementations. The dotted vertical lines mark the extent of the suction region.*

A comparison of the longitudinal pressure development at three different heights over the two different suction zone implementations can be seen in Figure 3.14. For all three heights, the custom boundary condition used in the full-scale simulations overpredicts the pressure rise over the suction region. This could be mitigated by adjusting the mass flow to result in the same pressure increase as for the perforated plate. Furthermore, it can be seen that the overall behavior of the pressure profile is correctly predicted by the custom boundary condition, which is a good indication of the validity of the model.

For validation of the tangential blowing modeling, displacement thickness data obtained from empty test section simulations and physical measurements were compared. The data were sampled 800 mm downstream of the front left tangential blower at a freestream velocity of 140 km/h and can be seen in Figure 3.15. It can be seen that the region outside the region influenced by the tangential blowing, $|y| \gtrsim 1150$ mm, is well predicted and that the overall behavior of the displacement thickness profile is captured by the simulations, including a slight reduction of the boundary layer caused by the upstream wheel drive unit. However, the bumps seen around the edges of the WDU belt are not seen in the simulation, which is also the case for the severe boundary layer thickening close to the center belt. It is believed that these differences are caused by that the floor is completely flat in the simulation, meaning that the interference between the moving belts and the stationary floor is not fully resolved. Furthermore, this simplification also removes the leakage flow that might occur between the test section and underfloor balance room in the physical tunnel, which, if directed into the test section, could result in a similar increase of the displacement thickness as seen in the measurement data.

Even though the numerical simulations well predict the overall behavior of the displacement thickness profile, it is possible that the velocity profile throughout the boundary layer behind the blowers is not. However, it is believed that such a discrepancy would be local and that the displacement thickness is a good measure of the global impact from the tangential blowers on the flow field.

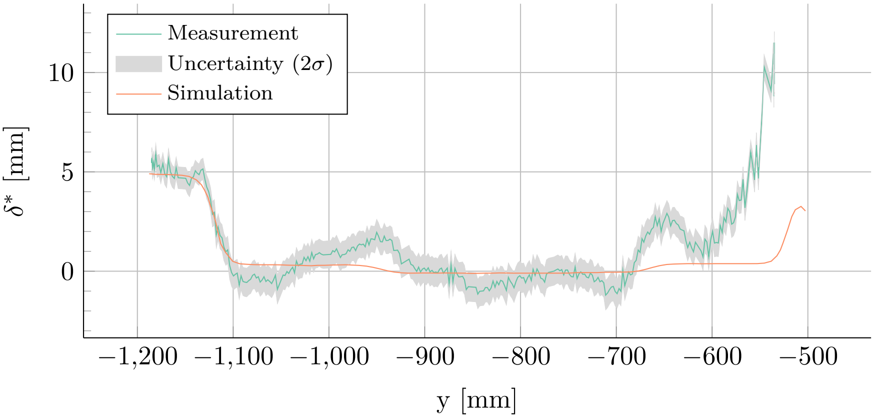

Figure 3.15: *Comparison of the displacement thickness between numerical simulations and measurements 800 mm behind the front left blower in the empty tunnel.*

3.2 Investigations of interactions between tunnel and test object

The flow around the test object is affected by the wind tunnel in numerous, ways which are often hard to separate and quantify. In this work, two such interactions have been investigated; the influence from the tangential blowing system on the measured aerodynamic forces, and the impact on these forces from flow angularity.

3.2.1 Influence of tangential blowing on vehicle configurations[1]

The influence from the tangential blowing system on the forces measured on two vehicles, a sedan Volvo S60 and a squareback Volvo V60, was investigated for the seven different parameters shown in Table 3.3. The cars were chosen to be as similar as possible except for the different rear end geometries since preliminary measurements had indicated that the rear end shape might influence the sensitivity to the tangential blowing. The investigated parameters were the same for both cars, except that the bootlid spoiler on the sedan was substituted for aero blades on the squareback. Some of the tested configurations can be seen in Figure 3.16. These specific factors were chosen since they were expected to influence the flow in the wake and/or under the car, which were the two regions expected to be mostly influenced by the tangential blowing. The reference configuration was chosen as the configuration with the expected highest drag and was the same for both vehicles: high ride height, open cooling, and no aerodynamic add-ons.

The investigation was performed using a 2^{7-3}_{IV} fractional factorial design of experiments approach, which allowed for quantification of both main effects and two-factor interactions [69]. However, since the design was of resolution IV, two-factor interactions were

---

[1] Large parts of this section have been carried over from the Licentiate thesis [8]

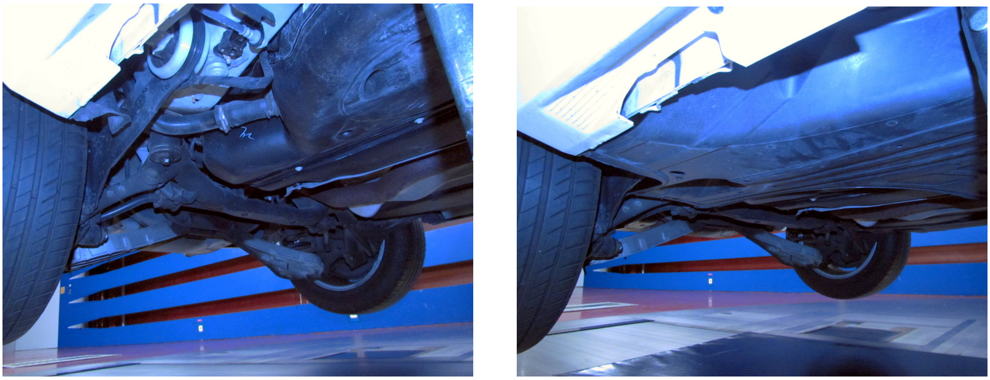

(a) *Underfloor panels off* (b) *Underfloor panels on*

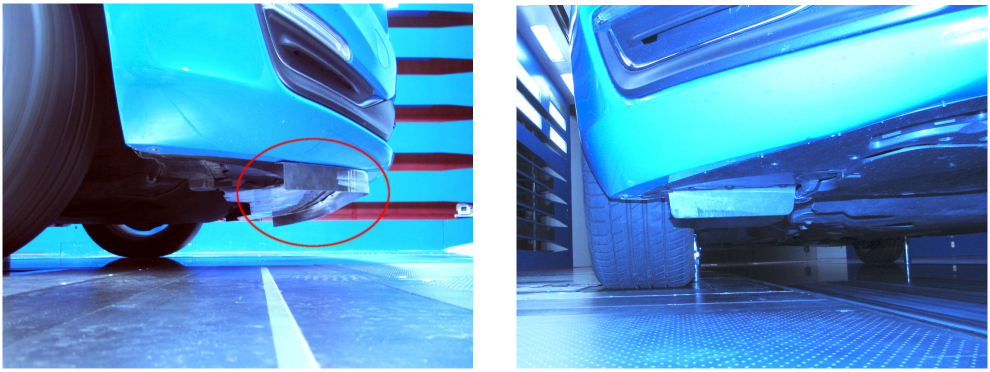

(c) *Air dam* (d) *Front wheel deflector*

(e) *Aero blades (squareback only)* (f) *Bootlid spoiler (sedan only)*

Figure 3.16: *Some of the configurations tested during the investigations on the influence of tangential blowing on the measured aerodynamic forces.*

Table 3.3: Factors investigated for the study on the influence of the tangential blowing system, their encodings and their levels in the experimental design. Ride height is given relative to the trim height at curb+2 weight.

Factor	Encoding	Low level	High level
Ride height	A	−15 mm	0 mm
Bootlid spoiler/aero blades	B	Off	On
Air dam	C	Off	On
Underfloor panels	D	Off	On
Front wheel deflectors	E	Off	On
Covered rims	F	Off	On
Cooling flow	G	Closed	Open

confounded with each other and could not be individually estimated. The confounding pattern for the design is shown in Table 3.4, where it can be seen that for example the interaction between ride height and bootlid spoiler/aero blades (AB) was confounded with the interactions between air dam and front wheel deflectors (CE), as well as covered rims and cooling flow. This meant that only the sum of these interactions could be estimated, but not their individual values. This limitation was the price paid for the low number of test runs, 16, required by the chosen design. In order to allow for individual estimation of all two-factor interactions, a design of resolution V would be needed, which would require 64 runs. This fourfold increase in the number of runs was not feasible since it would not be possible to fit into the wind tunnel time allotted for this investigation.

The aerodynamic forces on the car were measured for each run, both with tangential blowing on and off, after which each force coefficient was compared to its counterpart for the baseline configuration with the same blowing setting. This resulted in two delta values to the baseline for each configuration; one with tangential blowing on, and one with

Table 3.4: Confounding structure for the two factor interactions in the employed 2^{7-3}_{IV} fractional factorial design.

Interaction	Confounding structure
AB	AB + CE + FG
AC	AC + BE + DG
AD	AD + CG + EF
AE	AE + BC + DF
AF	AF + BG + DE
AG	AG + BF + CD
BD	BD + CF + EG

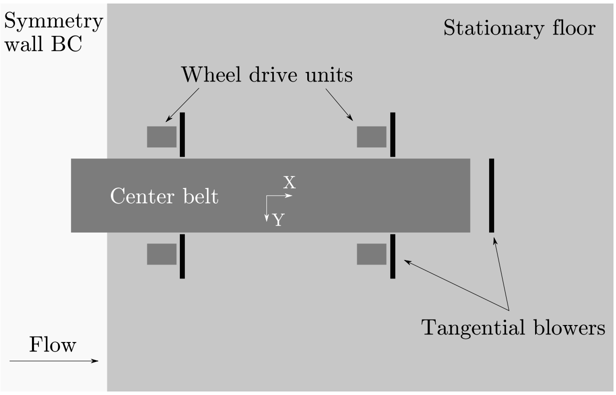

Figure 3.17: *Moving ground system as modeled for the tangential blowing investigations.*

blowing off. When investigating the sensitivity of the different parameters to the blowing, the interesting response to look at is the delta-of-deltas, i.e., the difference between the two deltas. In this way, the response will be zero for a parameter if its influence on the aerodynamic force is the same regardless of the tangential blowing setting.

Numerical simulations

Numerical simulations were used to find the local impact of tangential blowing on the vehicle surface. As for the empty wind tunnel simulations, the IDDES formulation of the SST $k - \omega$ model was used to model turbulence. However, the full geometry of the wind tunnel was not included; instead, a simple rectangular box was used. The moving ground system was represented by the five moving belts and their corresponding tangential blowers, as shown in Figure 3.17. The upstream suction systems were omitted, and an incoming boundary layer was avoided by using a symmetry boundary condition for the upstream section of the ground. Both the moving belts and the tangential blowers were modeled as in the empty test section simulations, and the rotation of the wheels was simulated using the Moving Reference Frame (MRF) approach.

The mesh consisted of 77 million trimmed cells, using 12 prism layers with a near-wall thickness of 0.0075 mm to 0.025 mm on the upper body of the car to resolve the boundary layer to $y^+ < 1$. On the underbody and in the engine bay, one 1 mm thick prism layer was built. The stationary part of the ground was covered with 8 prism layers with a near-wall thickness of 1 mm, accompanied by an anisotropic refinement of the cells close to the ground to account for the boundary layer buildup. The mesh on the center plane of the car can be seen in Figure 3.18.

The temporal resolution was $\Delta t = 2.5 \times 10^{-4}$ s, which yielded a CFL number below unity in the majority of the domain. The flow was initialized with a steady-state solution and allowed to develop for 2 s before averaging for 3 s, which corresponds to around 25 flow passes over the car. As for the physical tests, the simulations were run at a wind speed of 140 km/h.

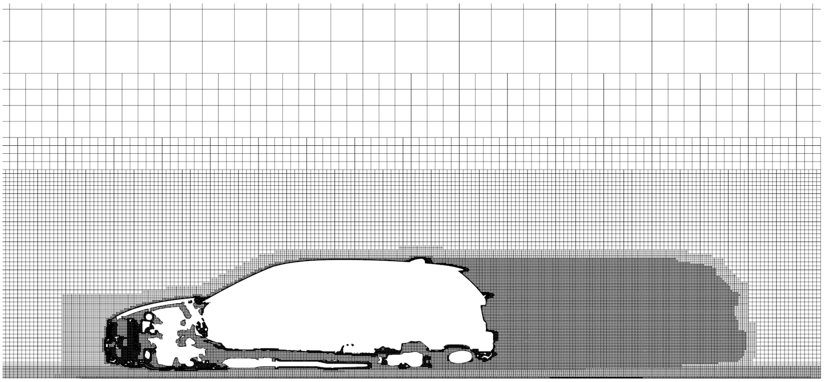

Figure 3.18: *Computational mesh at center plane of the squareback used for the tangential blowing investigations.*

3.2.2 Influence of induced flow angularity

To quantify the influence on the measured aerodynamic forces from the flow angularity induced by the taped turbulence screen described in Section 3.1.3, the reference vehicle that is used to perform regular checks of the wind tunnel repeatability was tested. The reference vehicle is a Volvo S80 sedan of model year 2008, and the tests were run as yaw sweeps from −20° to 20°, with one sweep run before adding the tape to the screen and one after.

3.3 Simulating vehicles inside the test section

The standard way of running numerical simulations for vehicle aerodynamics is to use so-called open road conditions, where the simulation domain is a large rectangular cuboid with uniform inlet flow, a fully moving ground plane, and negligible blockage. Unfortunately, these conditions cannot be exactly replicated in a physical wind tunnel, in which the data used for validating the simulations are typically gathered.

Although corrections are applied to the physical wind tunnel force measurements in order to account for the various interference effects introduced by the tunnel, these are applied at a global level and do not account for local effects. Furthermore, the correction methods are often based on inviscid flow theory and typically employ numerous simplifications and assumptions about, for example, the relation between the wake size and vehicle type.

Hence, to validate the accuracy of the numerical setup, a viable approach is to use the same boundary conditions in the simulations as in the wind tunnel. This means including the wind tunnel test section and its ground effect simulation system in the numerical simulations and comparing to uncorrected measurement data.

3.3.1 Experimental setup

In order to provide validation data for the simulations described later in this section, the two different vehicles shown in Figure 3.19 were tested; a Volvo S60 sedan of model year 2010, and a Volvo XC90 SUV of model year 2016. In order to simplify the numerical modeling of the wheel rotation in the numerical simulations, the sedan was equipped with slick tires with cut rain grooves, as described by Hobeika and Sebben [70]. Furthermore, it had been modified with a stiff suspension, removed drive shafts, closed cooling inlets, and taped split lines, as previously described by Hobeika [71] and Bonitz [72]. Apart from its baseline configuration, the sedan was also tested without its front wheel deflectors, with covered rims, and without rearview mirrors.

As for the sedan, the SUV had its driveshafts removed to allow the wheels to freely rotate on the wheel drive units in the wind tunnel. However, no simplified tires were available for this vehicle, why production tires were used. In an attempt to simplify the numerical simulation setup and to remove uncertainties of the heat exchanger modeling for the cooling package, all tests were run with the cooling inlets taped shut, as shown in Figure 3.19b. Similar to the sedan, the SUV was tested in its baseline configuration as well as without front wheel deflectors, and with covered rims.

The sedan was instrumented with pressure taps on the tophat centerline and the base, while only the centerline pressure was recorded using 16 pressure taps attached with stickers for the SUV. For the sedan, 122 drilled and sticker taps were used, of which 40 on the centerline and 82 on the base. All taps were connected to PSI ESP pressure scanners, and data were averaged for 20 s.

3.3.2 Numerical setup

As for the empty test section simulations described in Section 3.1.5, the simulations were run in STAR-CCM+ using the SST $k-\omega$ IDDES turbulence modeling approach. The simulations were initialized with a steady-state RANS solution and were allowed to develop for 2.6 s before averaging for 1.4 s, equating to about 11 flow passes over the car. The time step was 2.5×10^{-4} s, which resulted in CFL < 1 in the majority of the domain, with a small number of cells with CFL > 50. As shown by Ekman et al. [73] for a similar simulation setup and Hobeika and Sebben [70] for the sedan test object, the temporal resolution is expected to yield similar accuracy as for shorter time steps. The rotation of the rims was introduced using a sliding mesh approach, while the tire rotation was modeled using a rotating wall boundary condition.

The computational domain used for the open road simulations was a 70 m × 40 m × 30 m rectangular box with a fully moving ground plane. The inlet condition was a uniform 140 km/h velocity profile, while the sides and top were symmetry planes, and the outlet condition a pressure outlet with zero gauge pressure. For the simulations of a vehicle in the wind tunnel, the full high-speed leg shown in Figure 3.12 was used, and the moving ground systems were simulated as described in Section 3.1.5.

The overall meshing strategy was the same as for the empty test section simulations, with the mesh consisting of trimmer cells and prism layers. For the vehicles, the surface cell

(a) *The sedan*

(b) *The SUV*

Figure 3.19: *The sedan and the SUV used for validating the in-tunnel numerical simulations.*

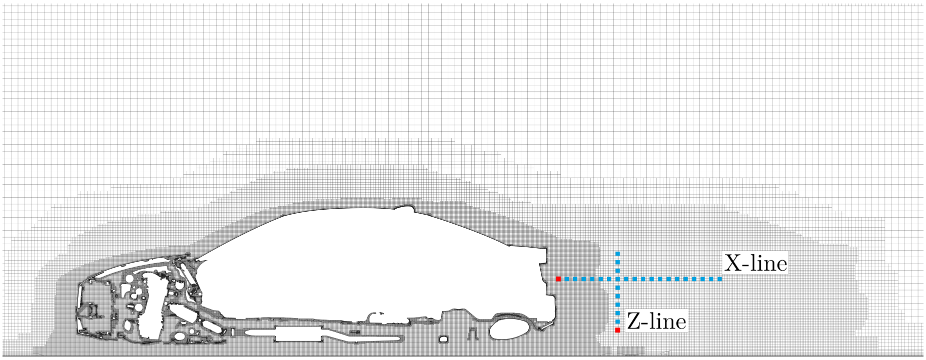

Figure 3.20: *View of the mesh on the center-plane around the sedan, with the two sampling lines used for the two-point correlation.*

sizes ranged from 1 mm to 8 mm on the tophat, underbody panels, and muffler, with up to 12 prism layers, resulting in $y^+ < 1$. For the rest of the underbody and the engine bay, the surface cell size was from 2 mm to 8 mm with one prism layer resulting in $y^+ < 130$. In order to resolve the base wake and wheel wakes, 8 mm cells were used in the volumetric refinements close to the car, and 16 mm cells further away.

For the open road simulations, this resulted in an overall cell count of approximately 135 million cells for the sedan and 260 million for the SUV. For the in-tunnel simulations, these numbers increased to 340 million cells for the sedan and 460 million for the SUV. The reason for this increase being larger than the total cell count in the empty tunnel simulations was that the trimmer mesher works by splitting cell sides in half for each refinement level. Thus only power-of-two multiples of the chosen base size are allowed. Since the already existing CFD setup that was used as the base for the vehicle simulations used a different base size than the empty tunnel simulations, it was decided to err on the side of caution and use slightly smaller cells throughout the wind tunnel when an exact match in cell size was not possible.

In order to evaluate the mesh resolution in the wake of the sedan, the two-point correlation approach proposed by Davidson [74] was used. This method uses the normalized two-point correlation of the velocity fluctuations

$$C^{\text{norm}}_{v'_x v'_x}(x_\text{A}, x_\text{B}) = \frac{\overline{v'_x(x_\text{A}) v'_x(x_\text{B})}}{v'_{x,\text{RMS}}(x_A) v'_{x,\text{RMS}}(x_\text{B})},$$

where v'_x denotes the fluctuating part of the longitudinal velocity v_x, and $v'_{x,RMS}$ its root mean square. The spatial coordinates of interest are denoted x_A and x_B, respectively, and the data was sampled along the two sampling lines shown in Figure 3.20, with the first point (marked in red) taken as x_A. According to Davidson [74], the largest eddies should be resolved by at least eight cells to achieve reasonable accuracy in LES simulations, which corresponds to $C^{\text{norm}}_{v'_x v'_x}(x_\text{A}, x_\text{B}) > 0$ for a separation distance between x_A and x_B of at least eight cells.

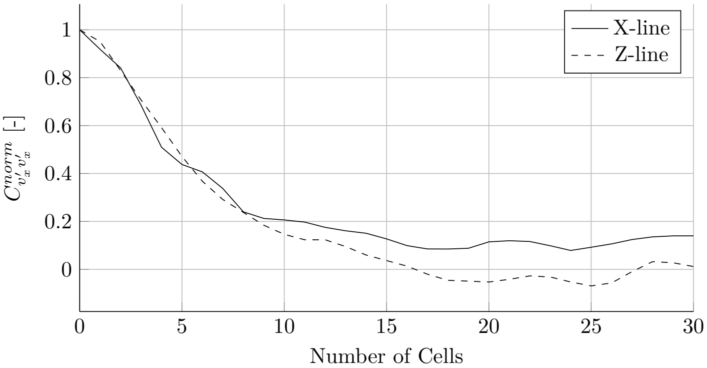

Figure 3.21: *Normalized two-point correlation for the sampling lines in the wake.*

As can be seen in Figure 3.21, the normalized two-point correlation spans more than 10 cells for both the sampling lines. Thus, it is concluded that the spatial resolution of the base wake is sufficient for the IDDES method, which is expected to work as an LES in this region.

Non-dimensionalization of forces and pressures

The process of non-dimensionalizing pressures and forces requires knowledge of the pressure and velocity in the freestream. For the open road simulations, the velocity on the inlet and the pressure on the outlet were used. However, the inlet mass flow tuned to achieve a certain velocity in the empty test section will result in a different velocity if applied to a simulation of a vehicle inside the test section. To solve this, the mass flow can be iteratively changed to result in the same pressure drop over the nozzle as the empty tunnel simulations, or the actual test section velocity can be calculated from this pressure drop. Here, the latter approach was used, and the freestream velocity was calculated as

$$u_\infty = \sqrt{\frac{2k_\mathrm{q}\Delta P}{\rho}}, \tag{3.4}$$

where k_q is a calibration constant from the wind tunnel commissioning, ΔP the pressure loss over the nozzle as measured by two pressure taps located in the settling chamber and near the nozzle exit, and ρ the air density.

Due to the test section pressure losses and the pressure recovery in the diffuser, the test section reference pressure will be significantly different from the pressure on the domain outlet. Thus, the test section reference pressure was also calculated based on the nozzle pressure drop as

$$P_\mathrm{s} = P_\mathrm{C2} + k_\mathrm{p}\Delta P,$$

where P_C2 is the pressure measured by the pressure tap at the nozzle exit, and k_p is another calibration constant from the commissioning. The way these two reference quantities are calculated corresponds to how they are determined in the physical tunnel, with the difference that (3.4) was adjusted to reflect the fact that the simulations treated the air as incompressible, whereas the physical tunnel takes compressibility into account.

Inclusion of the lift acting on the wheel drive units

In the physical measurements, the pressure field on the test section side of the wheel drive units is altered by the presence of the wheels. Thus, the whole WDU si subjected to a spurious lift force proportional to the pressure difference between the top and bottom surfaces of the wheel drive unit.

In order to achieve a one-to-one comparison between uncorrected physical test data and the in-tunnel simulations, the pressure was averaged over the WDU patches in the simulations and added to the front- and rear lift forces on the vehicle. This procedure assumes that the pressure acting on the lower side of the WDU equals the reference pressure in the test section. In the physical tunnel, a small difference has been measured between these pressures, which would amount to an error on the order of one lift count.

4 Results and discussion

This chapter covers the findings of the investigations presented in the preceding chapter, following the same division into the empty test section, interactions between the tunnel and the test object, and simulations of a vehicle inside the test section.

4.1 Empty test section investigations

This section presents and discusses the findings of the empty test section flow investigations. It covers the longitudinal pressure distribution and spatial uniformity of the tangential blowers, as well as flow uniformity in terms of static pressure and flow angularity on the turntable center plane.

4.1.1 Longitudinal pressure distribution

The longitudinal pressure distribution on the test section centerline can be seen in Figure 4.1, for two different operating modes of the boundary layer control system. In the aerodynamic mode, all sub-systems are activated, while only the basic suction scoop is running in the scoop only mode. It is evident from the figure that the wind tunnel fulfills the WLTP requirement of $\Delta C_p \leq 0.02$ between $x = -3\,\mathrm{m}$ and $x = 3\,\mathrm{m}$, for both operating modes. However, only the aerodynamic mode is interesting from a WLTP perspective since a moving ground is required.

Considering the aerodynamic mode, it is clear that the CFD method fails to predict the pressure development upstream of the turntable center. Since the pressure is much better predicted for the scoop only mode, it is likely that the fault lies in the modeling of either the distributed suction, moving belts, or the tangential blowing. Of these, only the distributed suction is expected to influence the longitudinal pressure gradient. As noted in Section 3.1.5, the custom boundary condition used for the distributed suction does not exactly predict the pressure drop over the distributed suction regions, which would indicate that a different mass flow should be used. However, changing the mass flow with up to 30 % did not turn out to lead to a significant change in pressure development in the upstream region of the test section. This might be an indication that the model used for the distributed suction is not able to represent the global influence from the suction through the perforated floor.

It has also been hypothesized that the wind tunnel geometry used in the simulations might not be an exact match of the physical tunnel. Thus, the wind tunnel was 3D-scanned, and the geometries compared. This comparison showed that one of the return flaps, which guides flow that has escaped into the plenum back into the main airline at the end of the test section, was misaligned. Adjusting the return flap in the numerical wind tunnel did not affect the test section pressure distribution. This is in line with the findings in the original commissioning [50, 51], where the flap open area ratio was varied from 0 % to 48 % with an influence seen only in the downstream part of the test section. Hence, it is expected that a small change around the standard open area ratio of 30 % does not have

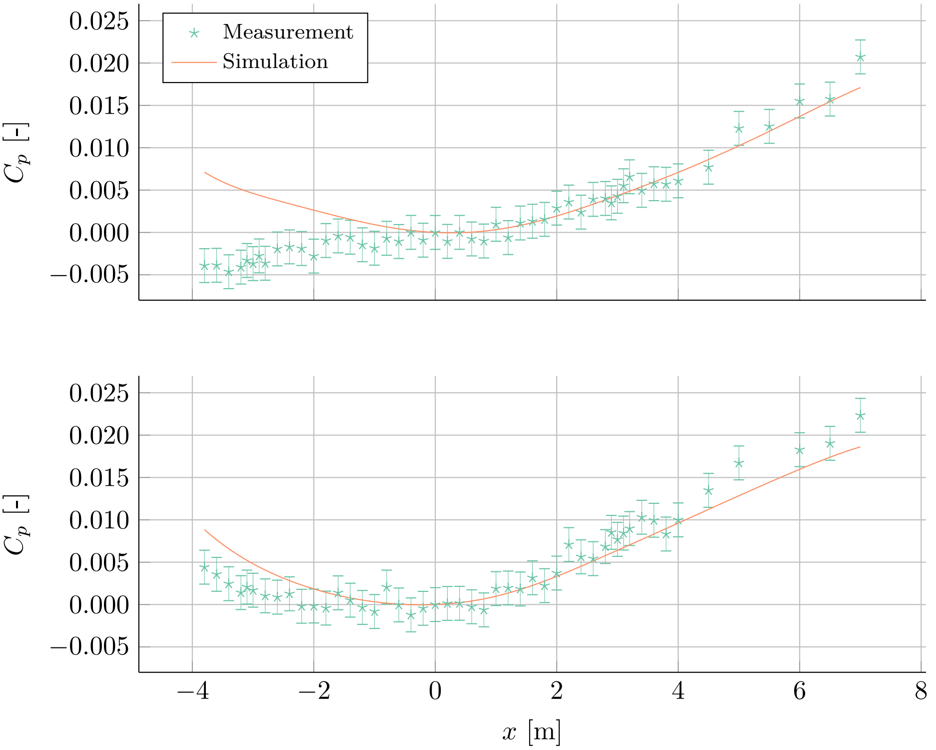

Figure 4.1: *The longitudinal pressure gradient from measurements and simulations for the aerodynamic mode of operation (top) and the scoop only mode (bottom) for the boundary layer control system. Note that all data have been offset such that* $C_p(x = 0) = 0$.

an impact on the upstream pressure development. However, all subsequent simulation data using the wind tunnel geometry are presented with the return flap in its correct position.

4.1.2 Tangential blowing uniformity[1]

The displacement thickness behind each wheel drive unit blower can be seen in Figure 4.2. Each blowing slot spans the region $520\,\mathrm{mm} \leq |y| \leq 1120\,\mathrm{mm}$, and the the shaded regions indicate the positions of the upstream WDU belts. When comparing the regions outside the influence from the blowers, $|y| \gtrsim 1150\,\mathrm{mm}$, it can be seen that the boundary layer grows as expected over the stationary floor between the front and rear measurement positions.

Adding to the difference between front and rear, there is also an asymmetry between the left and right blowers, which is especially evident close to the center belt for the front blowers. It is believed that the difference is more pronounced in this region due to a part

---

[1] Large parts of this section have been carried over from the Licentiate thesis [8]

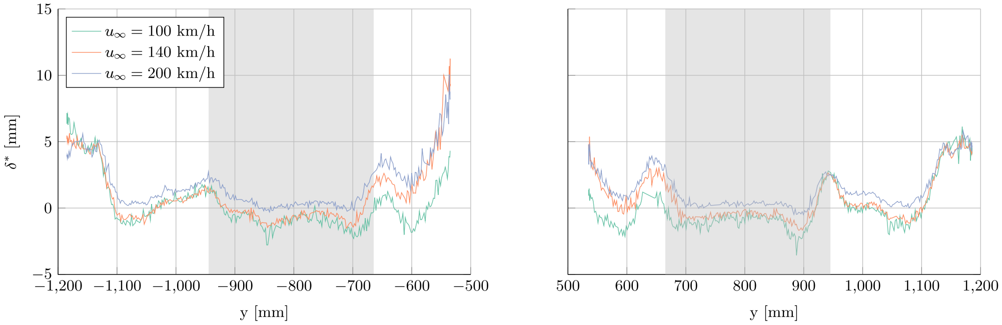

(a) *Front left*

(b) *Front right*

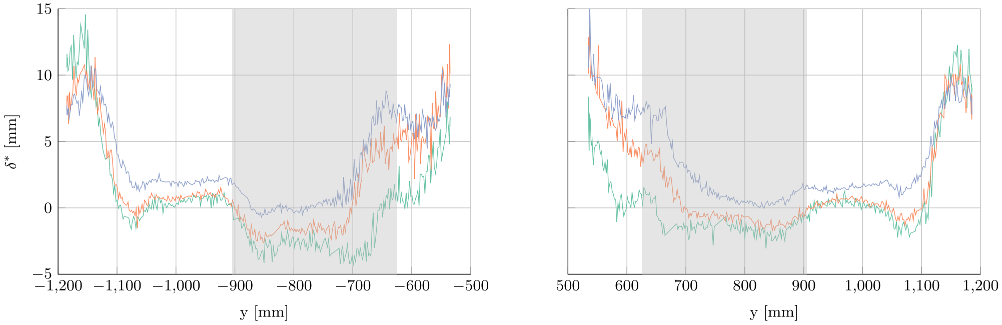

(c) *Rear left*

(d) *Rear right*

Figure 4.2: *Displacement thickness across the blowing slot 800 mm behind each wheel drive unit blower with the boundary layer control system in aerodynamic mode. The shaded areas mark the position of the upstream WDU belt.*

of a nylon strip that was previously acting as a spacing between the center belt and the surrounding stationary ground but has fallen off piece by piece. The part believed to cause the sharp rise in displacement thickness close to the center belt for the front left blower can be seen just upstream of the rake in Figure 3.2.

As mentioned in Section 3.1.5, a bump in the displacement thickness can be seen downstream of the edges of the wheel drive units for the front blowers. It is believed that this phenomenon is caused by a three-dimensional swirl originating from the interfaces between the stationary ground and the moving WDU belts, together with leakage flow entering the test section from the balance room through the gaps around the belt installations. This would also explain the increase in boundary layer thickness seen close to the center belt, i.e., for small $|y|$.

Considering the overall effect from the tangential blowing for all four blowers in Figure 4.2, it can be concluded that the tangential blowing system is effective at reducing the displacement thickness aft the wheel drive units. For the two lower velocities, the displacement thickness even becomes negative in some regions, mainly behind the WDU belts, which helps in reducing the boundary layer thickness upstream of the blowers. This would mean that the blowing speed should ideally be reduced, but since the displacement thickness profile is non-uniform, this would lead to a less effective boundary layer reduction in other areas. It can also be noted that the 200 km/h case shows consistently higher values for the displacement thickness for all four investigated blowers. This is likely because, at such high freestream velocities, the tangential blowing system is very close to its maximum capacity.

4.1.3 Flow uniformity

The static pressure uniformity on the turntable center plane ($x = 0$) can be seen in Figure 4.3. It can be seen that the probe measuring at $z = 1100\,\text{mm}$ measures a higher pressure compared to its neighboring probes, which results in a large and likely spurious gradient. This is believed to be caused by a faulty pressure hose, highlighting the importance of continually post-processing measurement data during the experiments. Doing so would have made it possible to fix the problem without having to re-run the full measurement campaign.

Comparing the three velocities, it can be seen that the static pressure coefficient is not significantly affected by the wind speed, except for the suspected faulty measurements at $z = 1100\,\text{mm}$. Even if those measurements are disregarded, the pressure profile is not entirely uniform, with a lower pressure seen on the upper half on the starboard side compared to the port side. It is not evident why this difference occurs, but it is consistent with the commissioning data after the moving ground and fan upgrade [49].

Similar to the static pressure, the flow angularity does not exhibit a dependence on wind speed, as can be seen in Figure 4.4. As there have been no major modifications to the airpath since the upgrade, it would be expected to find very similar flow patterns in Figures 4.4 and 2.8b. However, a significant difference can be seen in the upper half of the starboard side, where the inward and downward flow seen in 2006 is not visible in the present data. This makes the present measurements more similar to the original commissioning data in Figure 2.8a. In order to find the reason for this, all of the measurement planes for the 2006 data [49] were examined. All planes show a similar flow pattern for the upper half of the starboard side, and for the most upstream planes, the whole starboard half has a strong in- and downwash. The clear difference between the two lateral halves for the most upstream plane does not appear to be physical, and it is believed that this was caused by issues with the references used for the optical measurements of the probe mounting angles. These measurements were performed using a total station, which was likely mounted on different sides of the test section, depending on the lateral position of the vertical strut. Hence, it is plausible that different reference points were used to establish the position and orientation of the total station for the two lateral halves, thus causing the observed offset of the angles if one set of reference points were misplaced.

Further differences in pitch can be seen both in the uppermost and lowermost parts of the measurement region. These most likely stem from the fact that the commissioning strut

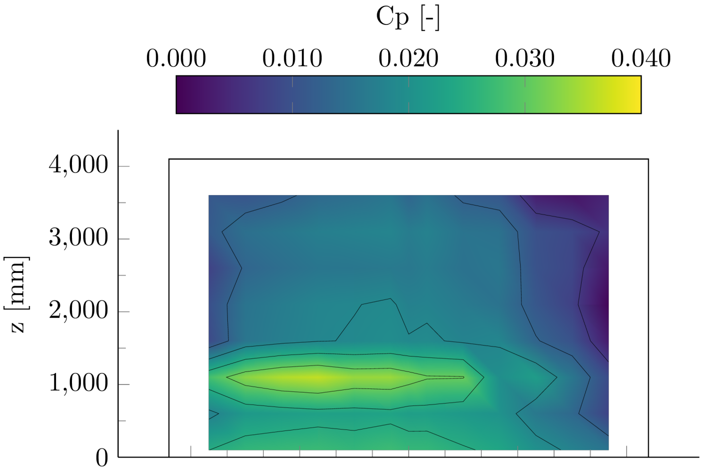

(a) *100 km/h*

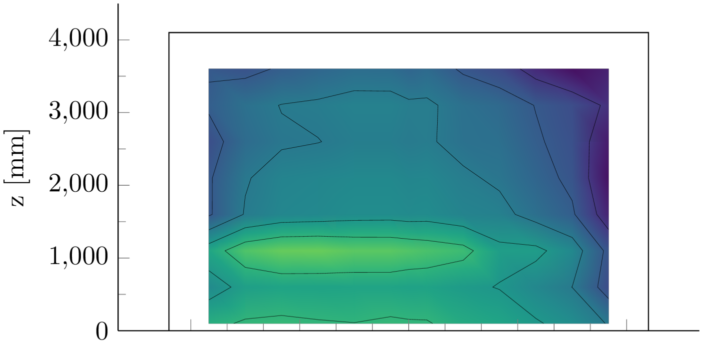

(b) *140 km/h*

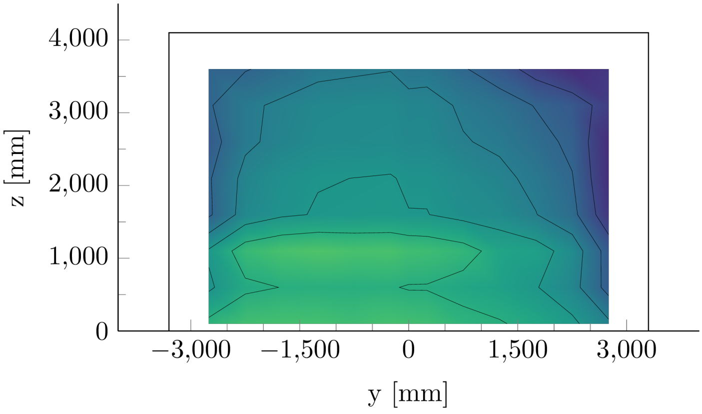

(c) *200 km/h*

Figure 4.3: *Static pressure uniformity at the turntable center plane.*

used in 1986 and 2006 interfered with the flow in these regions. The vertical part of the commissioning strut was hanging from a roof beam fastened in the slotted roof and secured at the bottom by a beam laid down on the floor, and both these beams would deflect the flow. Furthermore, since the overall flow interference from the old commissioning strut was larger than for the new flow measurement rig due to a thicker structure and a shorter standoff distance between the probes and the leading edge of the vertical strut, it is concluded that the present data is more likely to be representative of the actual flow pattern. This is further strengthened by the fact that the present measurements are corrected for rig interference, which was not the case for the commissioning measurements.

Measurement uncertainty

The uncertainties for flow angularity and pressure coefficients are shown in Table 4.1. They differ slightly between the measurements since the sensitivity coefficients, i.e., partial derivatives, of the post-processing program depend on the measured values. For static and total pressure, they are well within the requirements in Table 3.1 on the variations the flow measurement rig should be able to demonstrate, while the uncertainties for the flow angularity are about 2 to 3 times smaller than the required resolution. As noted in Section 3.1.4, the estimate of the total station uncertainty is likely pessimistic, meaning that the true uncertainty of the flow angularity measurements is probably lower than indicated in Table 4.1.

It can be noted that the uncertainties of the flow angularity measurements are effectively constant over the velocity range, while the static pressure uncertainty decreases with increasing velocity. The reason for this is that the uncertainty of the angularity measurements is dominated by the uncertainty of the measurements performed using the total station. Since no such measurements are needed for the static pressure coefficient, the major contribution to its uncertainty is the pressure measurement system, resulting in a decreased uncertainty as the dynamic pressure used for the normalization increases.

Another important thing to note is that measurement errors, such as the suspected faulty pressure hose for the static pressure measurements, are not covered by the uncertainty quantification. In the framework used [64], it is assumed that such errors are discovered during the campaign, and the measurement repeated with the errors corrected.

Table 4.1: Uncertainty distribution as one standard deviation for flow uniformity measurements at the turntable center for three different velocities.

	100 km/h			140 km/h			200 km/h		
	Min	Mean	Max	Min	Mean	Max	Min	Mean	Max
$u(\alpha)$ [°]	0.067	0.067	0.070	0.067	0.067	0.069	0.067	0.067	0.068
$u(\beta)$ [°]	0.051	0.053	0.058	0.051	0.052	0.055	0.051	0.051	0.053
$u(C_{p,s})$ [-]	0.001	0.004	0.005	0.001	0.002	0.003	0.001	0.001	0.001
$u(C_{p,t})$ [-]	0.000	0.004	0.005	0.000	0.002	0.003	0.000	0.001	0.001

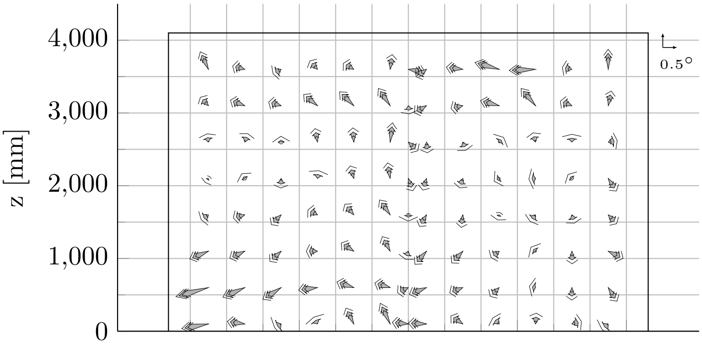

(a) *100 km/h*

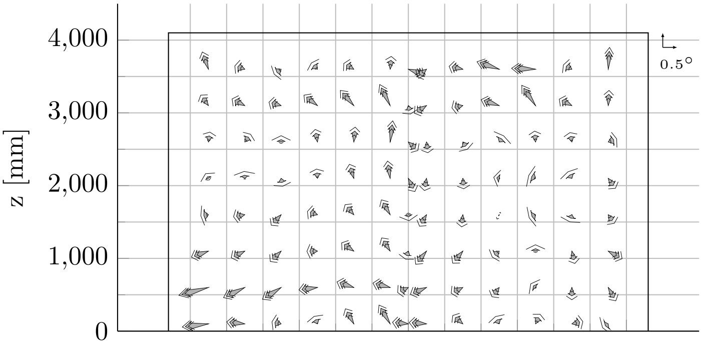

(b) *140 km/h*

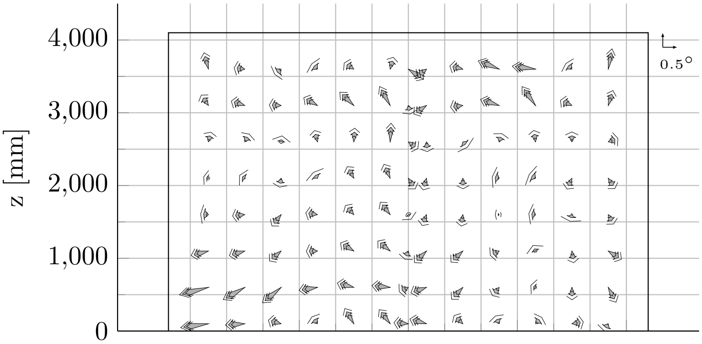

(c) *200 km/h*

Figure 4.4: *Flow angularity at the turntable center plane with uncertainties. The arrows in the upper right corner show the magnitude of 0.5° flow angularity in pitch and yaw.*

Influence from heat exchanger leakage and turbulence screen weld

Figure 4.5 shows the flow angularity for the standard operating conditions as well as with the modifications to the flow conditioning devices applied. Comparing Figures 4.5a and 4.5b, it can be seen that sealing the heat exchanger leakage does not impact the flow angularity in the test section. It is likely that the disturbance from the leakage flow is so small that it is dampened out by the three turbulence screens mounted downstream of the heat exchanger, and thus not result in any measurable impact on the test section flow field.

Turning to Figure 4.5c, it can be seen that adding the tape to the turbulence screen has a clear influence on the flow angularity at and around $y = 0$, but does not change the overall behavior of the flow pattern in a major way. Since the tape is significantly wider than the screen weld, the flow influence from the weld itself is much smaller than that caused by the tape. Thus, given that the overall influence from the tape is relatively small, it is concluded that the weld might have a minor influence on the flow angles at the lateral center, but that it is not a significant contributor to the swirling flow pattern in the test section. This is expected since the weld is very small compared to the total size of the settling chamber.

Since both the heat exchanger leakage flow and the screen welds have been ruled out as the cause of the rotating flow angularity pattern in the test section, the reason has to be found elsewhere. The fact that the rotation of the observed pattern corresponds to the rotational direction of the fan, and that the intensity of the rotation changed slightly when the fan was changed during the moving ground upgrade, indicates that the rotation stems from residual swirl from the fan. This corresponds well to the statement by Barlow et al. [24], saying that vortexlike flow patterns could be caused by non-uniform flow upstream of the third corner. In order to confirm this, measurements would have to be performed throughout the airpath of the tunnel.

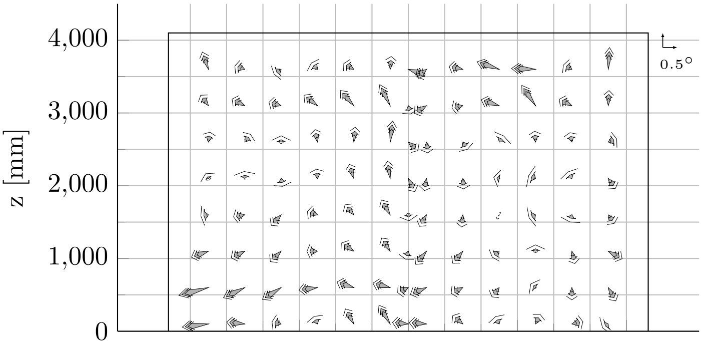

(a) *Baseline, standard operating conditions.*

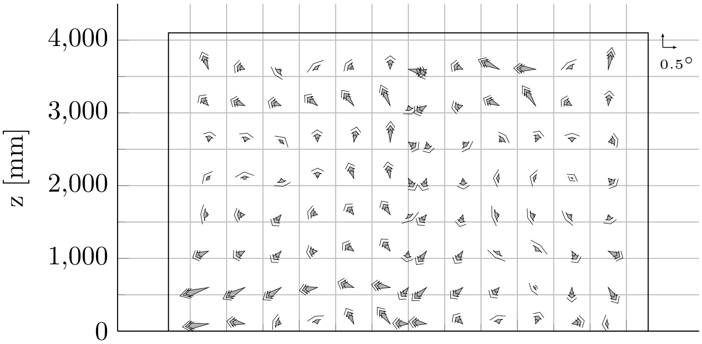

(b) *After sealing leakages around the heat exchanger.*

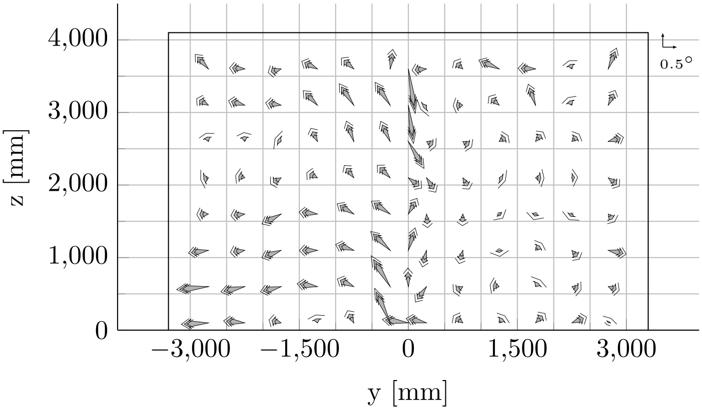

(c) *With tape on turbulence screen seam.*

Figure 4.5: *Flow angularity with uncertainties before and after modifications to the flow conditioning. The arrows in the upper right corner show the magnitude of 0.5° flow angularity in pitch and yaw.*

4.2 Interaction between tunnel and test object

This section treats the investigations into the tangential blowing system's impact onto measured forces in the wind tunnel, and how flow angularity in the test section affects the forces on a car.

4.2.1 Effect of tangential blowing on vehicle configurations[2]

The main effects and two-factor interactions on the measured force coefficient deltas and delta-of-deltas for both the notchback and the squareback can be seen in Figure 4.6. The horizontal black lines in the delta-of-deltas plots indicate the wind tunnel repeatability, as shown in Table 2.4, which is used to judge whether an effect is of significant magnitude or not.

Considering the effects for drag in Figures 4.6a and 4.6b, it can be seen that the squareback shows a considerably higher sensitivity to tangential blowing than the notchback. For the notchback, only the air dam (C) and closed cooling (G) show significant, however small, effects on the delta-of-deltas. These factors are also significant for the squareback, together with ride height (A) and front wheel deflectors (D). However, the magnitudes of the effects are much larger for the squareback, which is especially clear for the closed cooling, for which $\Delta\Delta C_D = 0.008$, or 47 % of the cooling drag measured with the blowing turned off. It is believed that the differences between the two vehicles are caused by the larger base area of the squareback, since the only major geometrical difference compared to the notchback is the shape of the rear end.

It can be noted that even though the effects for the delta-of-deltas change sign, the sign of ΔC_D compared to the baseline is not changed by the tangential blowing, except for the air dam (C) for both the notchback and the squareback. For this device, the small decrease in drag seen without tangential blowing vanishes when the blowing is turned on.

In contrast to the results for drag, the two vehicles show a similar sensitivity to tangential blowing for the front lift, as can be seen in Figures 4.6c and 4.6d. Both cars show a measurable sensitivity for the air dam (C) and the rim covers (F), as well as one interaction each; AD for the notchback and AB for the squareback. It can also be noted that the AD interaction shows a clear influence on ΔC_{LF} for both vehicles. Consulting the confounding pattern in Table 3.4 gives that this interaction also includes the interaction between the air dam and the closed cooling (CG), both of which show a large influence on ΔC_{LF}.

Even though some effects on $\Delta\Delta C_{LF}$ are larger than the repeatability of the wind tunnel, the differences between tangential blowing on and off are relatively small in comparison to the measured values for ΔC_{LF}.

Looking at the rear lift in Figures 4.6e and 4.6f, it can be seen that none of the effects for the delta-of-deltas are deemed significant by the employed criterion. This is partly due to the higher repeatability figures for rear lift compared to front lift.

---

[2] Large parts of this section have been carried over from the Licentiate thesis [8]

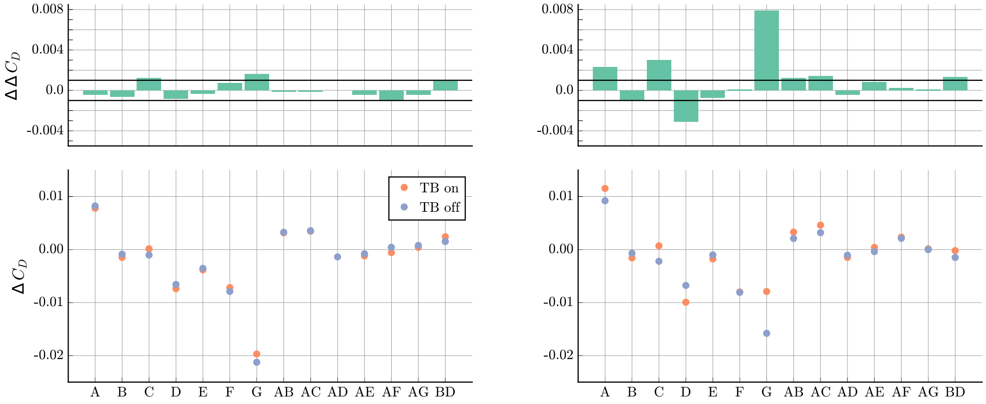

(a) *Effects on drag, notchback*

(b) *Effects on drag, squareback*

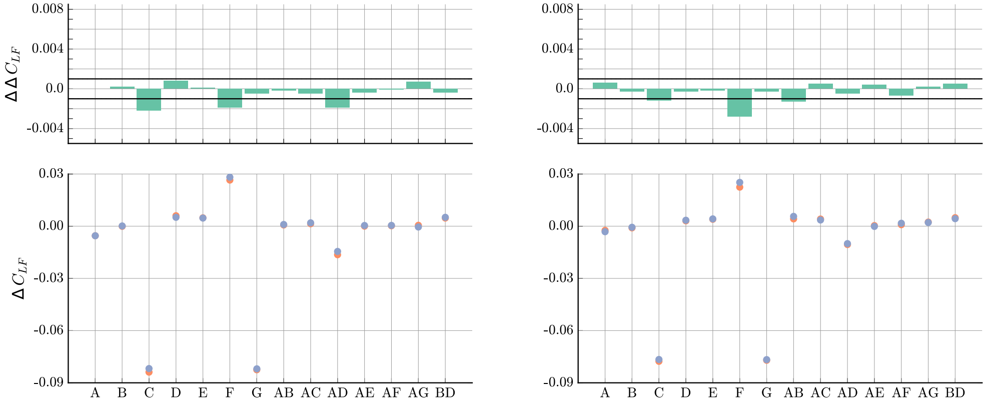

(c) *Effects on front lift, notchback*

(d) *Effects on front lift, squareback*

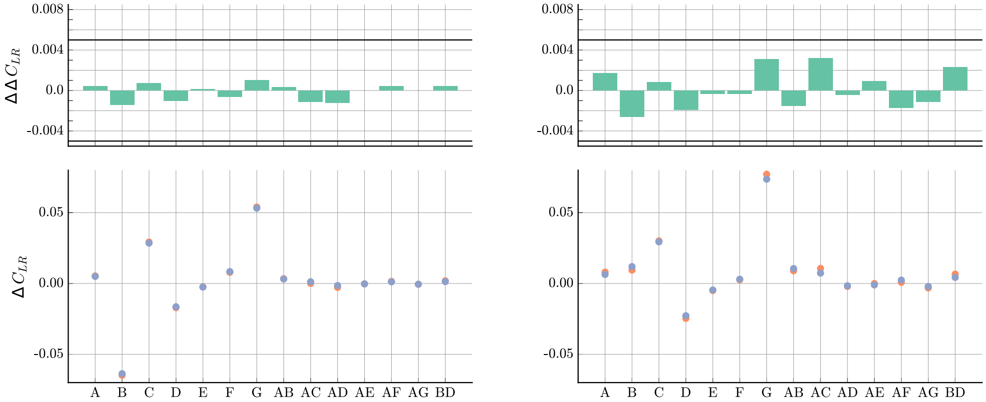

(e) *Effects on rear lift, notchback*

(f) *Effects on rear lift, squareback*

Figure 4.6: *Effects from tangential blowing on force deltas and delta-of-deltas. The horizontal black lines indicate the within-test repeatability of the wind tunnel.*

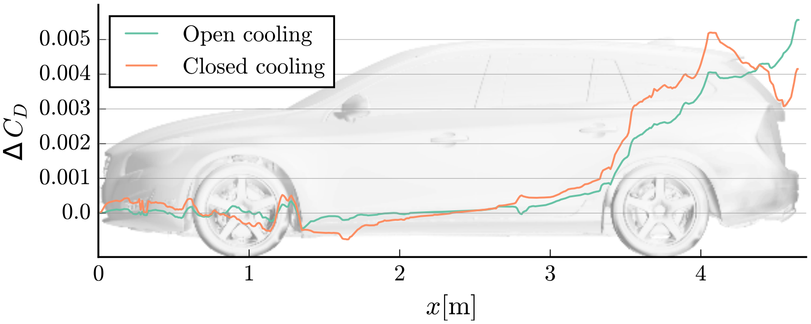

Figure 4.7: *Accumulated drag difference from CFD between tangential blowing on and off over the length of the car.*

The origin of the differences for the squareback

As previously discussed, the configuration most sensitive to tangential blowing is the closed cooling for the squareback. However, the force measurements in the wind tunnel give no guidance on where on the vehicle the differences occur, and how the flow field is affected by the tangential blowing. To investigate where the differences occur, the pairwise differences between four numerical simulations are analyzed. The four cases are all for the squareback, with open and closed cooling, and with and without tangential blowing.

In order to more clearly identify local differences between forces or in the flow field, a change of view is necessary compared to the physical tests. For the wind tunnel results, two drag deltas were defined, one for each blower mode. Using the closed cooling as an example gives

$$\begin{aligned}\Delta C_{D_{\text{closed, TB on}}} &= C_{D_{\text{closed, TB on}}} - C_{D_{\text{baseline, TB on}}}\\ \Delta C_{D_{\text{closed, TB off}}} &= C_{D_{\text{closed, TB off}}} - C_{D_{\text{baseline, TB off}}}.\end{aligned}$$

For the numerical simulations, one drag delta is instead used as

$$\Delta C_{D_{\text{closed}}} = C_{D_{\text{closed, TB on}}} - C_{D_{\text{closed, TB off}}}.$$

This is done in order to have results more similar in magnitude, thus facilitating identification of small differences.

In order to identify regions on the car that contribute to the drag difference observed in the wind tunnel, consider the accumulated drag difference along the length of the vehicle in Figure 4.7. Noting the difference between the curves at the downstream end of the car, it can be seen that the trend for $\Delta\Delta C_D$ seen in the wind tunnel (Figure 4.6b) is captured in the simulations. However, for the physical measurements $\Delta\Delta C_D = 0.008$, while $\Delta\Delta C_D \approx 0.002$ for the numerical model. This disagreement in magnitude between CFD and the wind tunnel is most likely a combination of multiple factors. For example, the numerical car model is not the exact same variant as the test object, and the full test section geometry is not included in the simulations. Furthermore, the simulations used slick tires, unlike the fully detailed tires used in the physical test, and the rim rotation was modeled using the MRF approach, which has been shown to result in less accurate simulations compared to a sliding mesh setup [71, 75].

Figure 4.7 shows that the major differences occur in the rear of the car, around the rear wheels and on the base. Considering the base, it can be seen that the trend shifts; while the tangential blowing decreases the drag contribution for the closed cooling, it slightly increases the contribution for the open cooling case. This effect is also noticeable when looking at the base pressure differences in Figure 4.8. For the open cooling, the tangential blowing slightly reduces the pressure on the right-hand side of the rear hatch, while it slightly increases the pressure on the left-hand side. These effects almost cancel out, which results in an almost flat curve in this region in Figure 4.7. Looking at the closed cooling case, it can be seen that the pressure is increased on most parts of the hatch, thus reducing the drag influence, as seen in the accumulated drag.

4.2.2 Influence of induced flow angularity

The force coefficient differences measured on the reference car between standard operating conditions and with the tape applied to the downstream turbulence screen can be seen in Figure 4.9. The error bars represent the within test repeatability given in Table 2.4. The reason for the double measurements at zero yaw is that the yaw sweep procedure is built up by two sub-procedures, each starting at zero yaw and measuring either the positive or negative angles.

From the figure, it can be seen that ΔC_D is within the in-test repeatability for most yaw angles, with a notable exception being the largest negative angles. However, the maximum delta is still within the between test repeatability. Considering the rear lift, the measured difference is within the in-test repeatability for all yaw angles. This is not the case for the front lift, which is consistently increased by $\Delta C_{LF} \approx 0.005$ over the full yaw angle range, except for the two largest positive angles. This increase is expected, given that the tape induces an upward flow in the lower central region of Figure 4.5c. However, both ΔC_D and ΔC_{LF} are within the between test repeatability of the wind tunnel throughout the full yaw angle range, and the force changes should thereby not be considered as substantial. Furthermore, the difference in flow angularity introduced by the tape is of a similar magnitude as the flow angularity under standard operating conditions. Thus, it is likely that the flow angularity present in the test section in standard operating conditions does not have a significant influence on the forces measured on a vehicle, compared to an ideal flow without angularity.

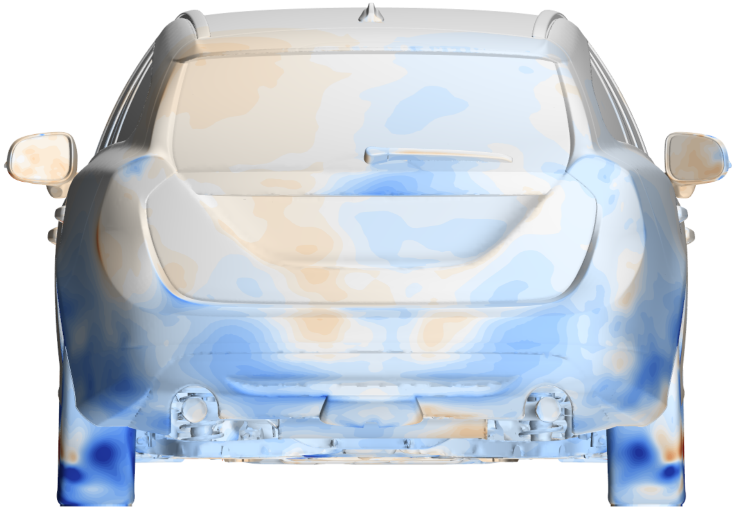

(a) *Open cooling*

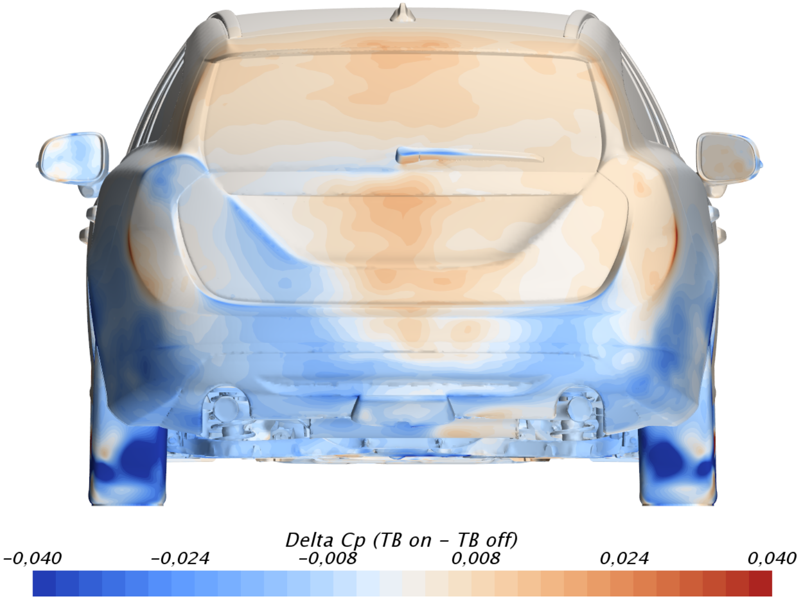

(b) *Closed cooling*

Figure 4.8: *Difference in pressure coefficient, ΔC_P, on the base of the squareback.*

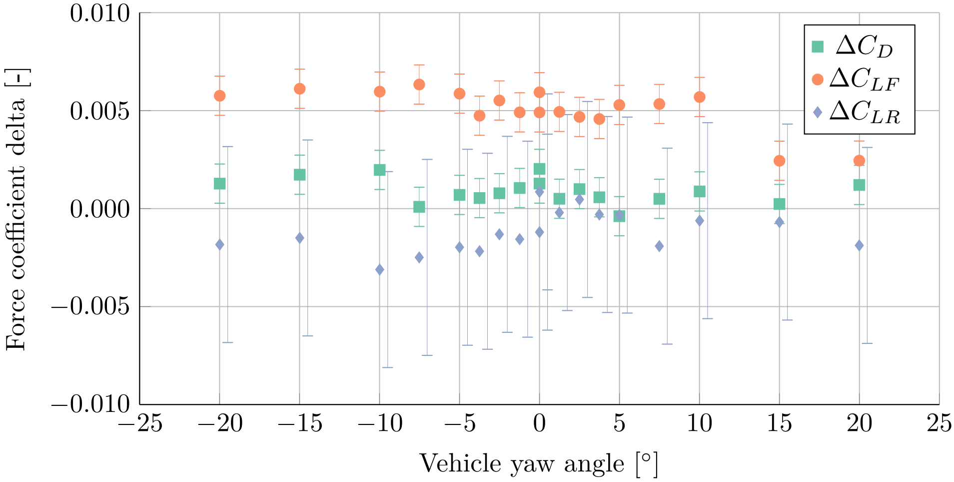

Figure 4.9: *Force coefficient deltas between the case with tape on the downstream turbulence screen and standard operating conditions for the reference vehicle over a yaw sweep.*

4.3 Simulating vehicles inside the test section

Here, the results of simulating a sedan and an SUV, both in open road conditions as well as inside the wind tunnel test section, are presented and discussed. A comparison of the force coefficients from physical measurements and the two simulation types can be seen in Figure 4.10 for the sedan and Figure 4.11 for the SUV. Each force coefficient presented has been given an arbitrary offset for confidentiality reasons. “Corrected PVT” and “Uncorrected PVT” denote physical measurements in the wind tunnel, with and without blockage corrections applied, while “Open road CFD” and “PVT CFD” denote simulations in open road conditions and with the wind tunnel test section as the simulation domain, respectively. “PVT CFD WDU” refers to values including the lift acting on the wheel drive units, as described in Section 3.3.2. For all forces and configurations, the open road CFD should be compared to the corrected measurement data and the wind tunnel CFD to uncorrected measurements.

Figure 4.10a shows that drag prediction for the sedan is significantly improved by including the wind tunnel geometry in the simulations for all investigated cases. For both the baseline case and the case without front wheel deflectors, the tunnel simulations result in a drag coefficient matching the uncorrected measurements. With covered rims, and for rearview mirrors removed, the tunnel simulations give drag values that are 5 counts higher than the uncorrected tunnel values. This is just outside the repeatability of the physical measurements, which is within 3 counts, as given in Table 2.4. The improvement in drag prediction aligns well with the results of the base pressure measurements displayed in Figure 4.12, where it can be seen that the base pressure from the open road simulations is overall higher than what is measured in the wind tunnel. For the in-tunnel simulations, the overall pressure is better predicted, even though some differences still occur, especially in

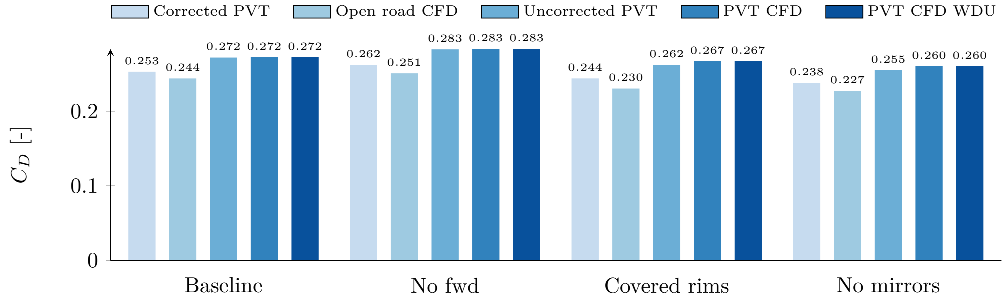

(a) *Drag*

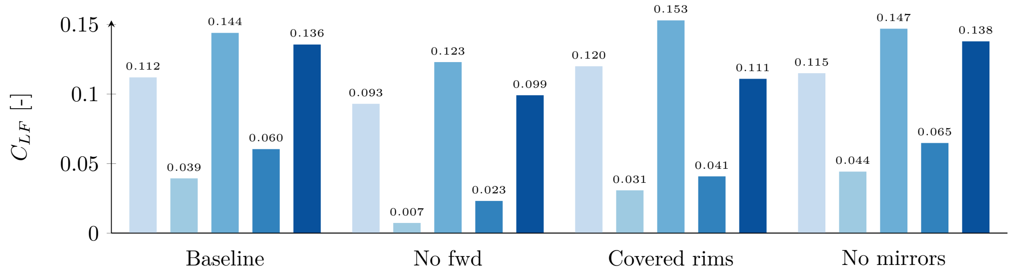

(b) *Front lift*

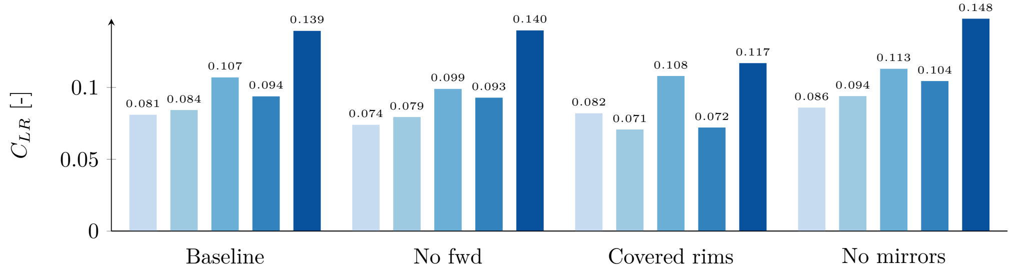

(c) *Rear lift*

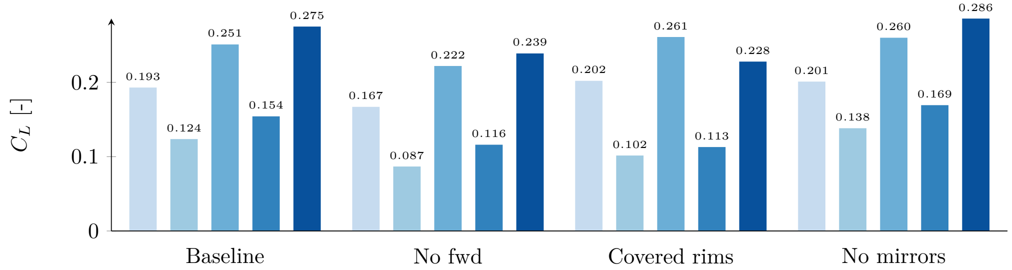

(d) *Total lift*

Figure 4.10: *Comparison of drag and lift coefficients between the wind tunnel and simulations for the sedan. All coefficients have been offset for confidentiality.*

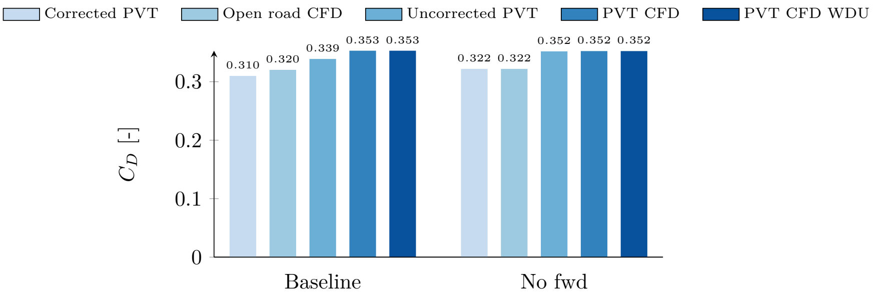

(a) *Drag*

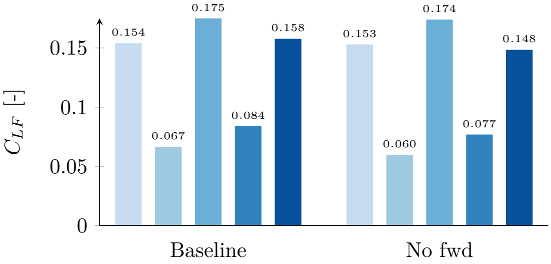

(b) *Front lift*

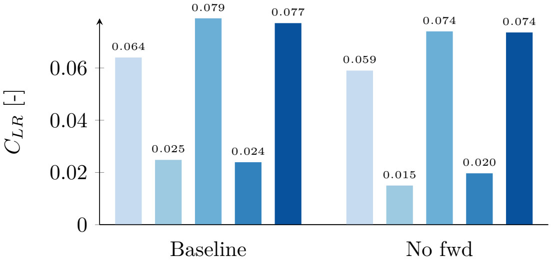

(c) *Rear lift*

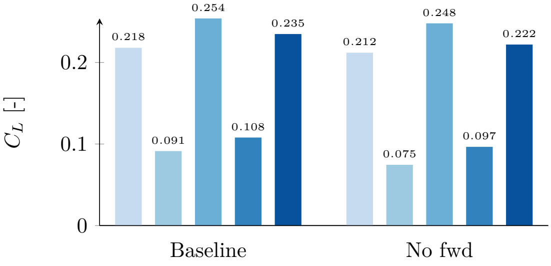

(d) *Total lift*

Figure 4.11: *Comparison of drag and lift coefficients between the wind tunnel and simulations for the SUV. All coefficients have been offset for confidentiality.*

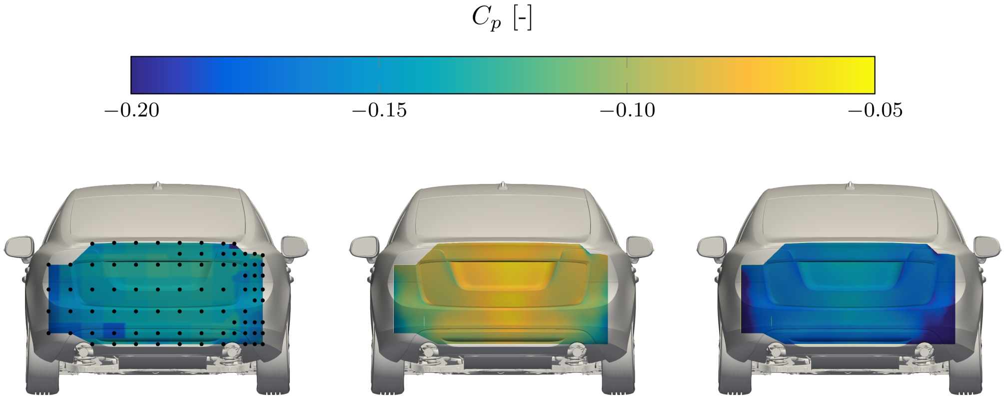

(a) *Physical measurement* (b) *Open road CFD* (c) *PVT CFD*

Figure 4.12: *Base pressure distribution on the sedan in its baseline configuration from measurements (a), and simulations (b) and (c).*

the lower right region where the simulations show a lower pressure than the measurements. This can be partly explained by the pressure taps being slightly misplaced in this area.

The drag prediction for the SUV in Figure 4.11a agrees with the wind tunnel data for the case without front wheel deflectors, both for the open road and in-tunnel simulations. However, the results are not as good for the baseline case, for which the open road simulation overpredicts drag with 10 counts, and the in-tunnel simulation overpredicts with 14 counts. Hence, the drag delta between the two configurations is not well predicted in either of the simulation domains.

The likely cause of the better prediction quality seen for the sedan is that the geometrical precision between the physical test object and the numerical model is superior compared to the SUV. For example, fully detailed tires were used for the physical SUV, whereas the numerical model introduced some simplifications. Even though the physical tires were 3D-scanned and morphed to achieve a representative profile, the tread pattern was simplified to only include the circumferential rain grooves in the simulations. As shown by Hobeika and Sebben [70], adding the lateral grooves in the simulations can have a measurable effect on drag. They also found that the drag increase seen when adding lateral grooves to a tire that already had circumferential rain grooves was located to the region around the front wheels, which is the area affected by the removal of the front wheel deflectors. This further strengthens the belief that the simplified tires might contribute to the worse prediction quality for the SUV. Furthermore, the rocker panel restraint struts holding the car in place in the wind tunnel were omitted from the simulations of the SUV by mistake, which most likely also influences the drag prediction for the in-tunnel simulations.

Considering the lift, Figures 4.10 and 4.11 show that the lift predictions are quite poor for both simulation domains when not including the WDU lift, with the rear lift for the sedan as an exception. Including the wind tunnel domain does not improve the lift predictions unless the suction on the WDU belts is taken into account. Doing so results in a significant improvement except for the sedan C_{LR}, which is severely overpredicted. This results in an overprediction of the total lift for the sedan, but an underprediction for the SUV. For the SUV, however, it is likely that the lift is also affected by the aforementioned simplifications of the tires, especially so for the pressure on the wheel drive unit belts. However, the closed rim configuration of the sedan is an exception with an underpredicted front- and total lift more similar to the SUV simulations. This can likely be attributed to a misprediction of the flow field close to the contact patch, affecting the pressure on the WDU belt and on the wheel itself. Previous studies have found that open road simulations have difficulties predicting the behavior of fully covered rims [70, 76, 77]. Hobeika and Sebben [70] hypothesized that the flow around the wheel is dominated by the rotating rim spokes for an open rim, while the tire sidewall has a larger influence for the closed rim. Hence, disregarding the roughness of the sidewall in the simulations, as in the current work, might result in a different flow behavior compared to the physical measurements.

Regarding the overpredicted lift for the sedan when including the suction on the WDU belts, it is likely that the contribution from the WDU belts is too large in the simulations. When the correction method for the physical method was developed, it was found that CFD simulations overpredicted the lift on the WDUs with around 20 % [30]. This was also in line with a previous study by Wickern and Beese [78]. It is thereby plausible that the present method suffers from the same problem, likely caused by the omittance of the gaps around the WDU installations. These gaps exist in the physical tunnel to allow the belts to rotate and to avoid unwanted load transfer between the WDU, which is connected to the underfloor balance, and the stationary floor. The gaps would allow for some leakage flow between the underfloor balance room and the test section, acting to reduce the pressure difference causing the lift on the WDU, and thereby reducing this lift contribution.

Considering the centerline pressures shown in Figure 4.13, it can be seen that the in-tunnel simulations generally result in a lower pressure, which is in line with the observed lift increase. For the sedan, the inclusion of the test section geometry results in a clear improvement of the centerline pressure prediction over the roof and rear window. However, the trend for the SUV is not as clear, although the in-tunnel simulations result in slightly better predictions over the roof of the car. It is interesting to note that the in-tunnel simulations seem to underpredict the pressure for the SUV, which is not the case for the sedan. A possible cause for this is that the higher blockage caused by the SUV forces more flow into the plenum through the slotted walls and roof. Since some details such as cables and some auxiliary equipment mounted in the plenum have been omitted from the simulations, it is possible that the blockage caused by these installations become significant with higher test section blockage ratios as for the SUV, and thus result in higher pressure buildup than captured in the simulations. This would also affect the drag predictions by altering the horizontal buoyancy experienced by the test object.

It is also likely that the difference in longitudinal pressure between the physical tunnel and the empty test section simulations discussed in Section 4.1.1 influences the results of the in-tunnel simulations. This difference most likely results in a slightly lower drag in the simulations compared to the uncorrected measurements since the horizontal buoyancy

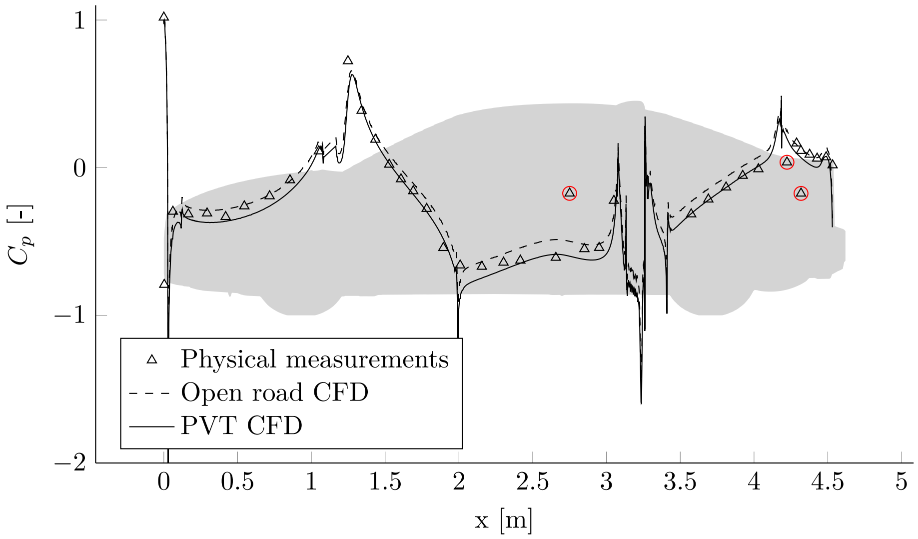

(a) *The sedan. The pressure taps marked with red circles are believed to be damaged.*

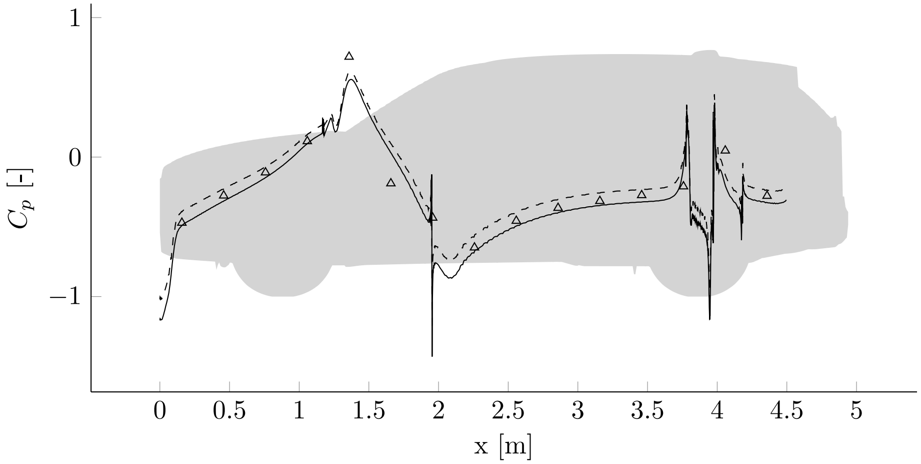

(b) *The SUV.*

Figure 4.13: *Centerline pressure on the tophat for the two vehicles in their respective baseline configuration.*

induced by the simulated pressure profile should be smaller than its physical counterpart. Furthermore, as the difference occurs upstream of the turntable center, it is also likely that the front lift is affected. This is further complicated by that in the physical wind tunnel, the suction through the perforated plates probably changes depending on the pressure field the test object imposes on the ground. Since the numerical model assumes a uniform flow over the whole suction surface, such an effect will not be captured in the simulations, further adding uncertainty on the pressure field in this region.

5 Summary and conclusions

This thesis has aimed at improving the understanding of the properties of a slotted wall wind tunnel used for automotive aerodynamic testing, as well as improving the prediction quality of numerical simulations. This has been done by investigations of the flow in an empty test section, as well as studies of both local and global interactions between the wind tunnel and the test object.

For the empty test section flow, it was shown that the wind tunnel fulfills the pressure gradient requirement set by the WLTP standard for vehicle certification. Furthermore, it was shown that the swirling flow pattern seen during the two previous commissioning campaigns is still present in the test section. Both leakage flow around the wind tunnel heat exchanger, as well as welds on the turbulence screens, were ruled out as the cause for this flow pattern, and it is instead believed to be caused by residual swirl from the fan. By artificially introducing flow angularity in the test section, it was shown that the flow angularity present in the empty tunnel during normal operation most likely does not have a significant effect on the forces measured on vehicles.

For the flow uniformity measurements in terms of flow angularity and pressure, it was shown that low measurement uncertainty could be achieved using standard five-hole probes and facility installed pressure scanners. This was achieved by calibrating the probes in-situ and tracking the contribution of all sources of uncertainty.

The numerical simulations of the empty test section flow were able to accurately predict the longitudinal pressure development in the downstream part of the test section. However, they were not able to satisfactorily predict the pressure in the upstream region when the Ground Effect Simulation System (GESS), including distributed suction, moving belts, and tangential blowers, was active. The prediction improved when deactivating the GESS in both the physical test and the simulations, which indicates that the modeling approach used for the distributed suction is not fully representative of the physical system, despite numerical tests showing that the general trend of the pressure development was captured by the simplified boundary condition used, when compared to resolving the perforated suction plates. Further investigations of the modeling of the distributed suction system would be desirable if a better prediction of the longitudinal pressure gradient is required.

An investigation of the tangential blower system showed that it is effective at reducing the displacement thickness of the boundary layer after the moving belts and that numerical simulations can well predict the overall behavior of the boundary layer behind a blower. It was also shown that a squareback type of car was more sensitive to tangential blowing than a similar sedan, and that configuration changes affecting the underbody flow were more sensitive than those only affecting the flow in the base wake. Furthermore, numerical simulations of the squareback indicated that most of the differences between tangential blowing on and off originated from the rear of the car, mainly around the rear wheels and the base.

By simulating two vehicles both in open road conditions and in the wind tunnel, it was found that the prediction of force coefficients and surface pressure could be significantly improved by using the test section as the simulation domain. This was achieved by computing the non-dimensionalized quantities for the in-tunnel simulations the same way as in the physical wind tunnel, meaning that the test section reference pressure and nominal test velocity were calculated based on the pressure drop over the nozzle.

Even doing so, some vehicle configurations were less accurately predicted, which was mostly attributed to uncertainties concerning the geometrical representation of the test object in the numerical model. This was especially true for the tires for one of the vehicles, which were simplified in the numerical simulations. The other tested vehicle had simplified tires in the physical test that could be accurately represented in the simulations, which resulted in overall better predictions of drag. It is thereby recommended that similar studies use tires that can be accurately represented in numerical simulations to reduce this uncertainty. Furthermore, it would be beneficial to run more vehicle types in different configurations, possibly in yawed conditions, and to perform flow field measurements to provide further validation of the setup.

An important finding of this thesis is that it is crucial to include the lift acting on the wheel drive unit (WDU) belts in the in-tunnel simulations in order to achieve reasonable lift predictions. However, it is believed that the current method overpredicts this lift contribution due to geometrical simplifications of the WDU installation. To verify this, experiments would need to be conducted where the lift acting on the WDUs could be measured, for example, by lifting the car to remove the contact with the belts and measure the forces with and without covers over the WDUs. Furthermore, it is likely that the prediction of the pressure field over the distributed suction system influences front lift, further accentuating the need for more investigations on how to represent this system in the numerical simulations.

A well-established numerical simulation method for the wind tunnel would allow for more investigations on how to make the physical tunnel as representative of the open road conditions as possible. This would be done by comparing numerical simulations of vehicles in the test section with those performed in open road conditions. For example, studies could be performed on whether the usage of tangential blowing improves the wind tunnel's simulation of the open road conditions or not. Another possibility would be to improve the correction methods used in the physical tunnel to better match the blockage free case.

References

[1] E. Ljungskog, S. Sebben, A. Broniewicz, and C. Landström. “On the Effects of Wind Tunnel Floor Tangential Blowing on the Aerodynamic Forces of Passenger Vehicles”. *SAE International Journal of Passenger Cars - Mechanical Systems* 10(2) (2017), pp. 591–599. DOI: `10.4271/2017-01-1518`.

[2] E. Ljungskog, S. Sebben, and A. Broniewicz. “Uncertainty Quantification of Flow Uniformity Measurements in a Slotted Wall Wind Tunnel”. *SAE Technical Paper 2019-01-0656*. Apr. 2, 2019. DOI: `10.4271/2019-01-0656`.

[3] E. Ljungskog, S. Sebben, and A. Broniewicz. “Flow Angularity Investigations in an Automotive Slotted Wall Wind Tunnel”. *Accepted for publication in Energies* (2019).

[4] E. Ljungskog, S. Sebben, and A. Broniewicz. “Inclusion of the Physical Wind Tunnel in Vehicle CFD Simulations for Improved Prediction Quality”. *Submitted to Journal of Wind Engineering and Industrial Aerodynamics* (2019).

[5] E. Ljungskog, S. Sebben, A. Broniewicz, and C. Landström. “A parametric study on the influence of boundary conditions on the longitudinal pressure gradient in CFD simulations of an automotive wind tunnel”. *Journal of Mechanical Science and Technology* 31.6 (June 1, 2017), pp. 2821–2827. ISSN: 1738-494X, 1976-3824. DOI: `10.1007/s12206-017-0525-2`.

[6] C. Kounenis, S. Bonitz, E. Ljungskog, D. Sims-Williams, L. Lofdahl, A. Broniewicz, L. Larsson, and S. Sebben. “Investigations of the Rear-End Flow Structures on a Sedan Car”. *SAE Technical Paper 2016-01-1606*. SAE 2016 World Congress and Exhibition. Apr. 5, 2016, pp. 2016–01–1606. DOI: `10.4271/2016-01-1606`.

[7] M. Urquhart, E. Ljungskog, and S. Sebben. “Surrogate-based optimisation using adaptively scaled Radial Basis Functions”. *Submitted to Applied Soft Computing* (2019).

[8] E. Ljungskog. “Investigations of Flow Conditions in an Automotive Wind Tunnel”. Licentiate Thesis. Chalmers University of Technology, 2017.

[9] J. G. Olivier, J. A. Peters, and G. Janssens-Maenhout. *Trends in global CO2 emissions; 2016 Report*. The Hague: PBL Netherlands Environmental Assessment Agency; Ispra: European Commission, Joint Research Centre., 2016.

[10] *United Nations Global Technical Regulation on Worldwide harmonized Light vehicles Test Procedure (WLTP)*. United Nations GTR ECE/TRANS/180/Add.15. Sept. 20, 2018.

[11] D. D. Baals and W. R. Corliss. *Wind Tunnels of NASA*. Washington, D.C.: National Aeronautics and Space Administration, 1981. 163 pp.

[12] K. E. Ludvigsen. “The Time Tunnel - An Historical Survey of Automotive Aerodynamics”. *SAE Technical Paper 700035*. Feb. 1, 1970. DOI: `10.4271/700035`.

[13] B. Chanetz. “A century of wind tunnels since Eiffel”. *Comptes Rendus Mécanique*. A century of fluid mechanics: 1870–1970 345.8 (Aug. 1, 2017), pp. 581–594. ISSN: 1631-0721. DOI: `10.1016/j.crme.2017.05.012`.

[14] G. Wickern and N. Lindener. “The Audi Aeroacoustic Wind Tunnel: Final Design and First Operational Experience”. *SAE Technical Paper 2000-01-0868*. Mar. 6, 2000. DOI: `10.4271/2000-01-0868`.

[15] J. Walter, E. Duell, B. Martindale, S. Arnette, R. Geierman, M. Gleason, and G. Romberg. “The DaimlerChrysler Full-Scale Aeroacoustic Wind Tunnel”. *SAE Technical Paper 2003-01-0426*. Mar. 3, 2003. DOI: `10.4271/2003-01-0426`.

[16] P. Waudby-Smith, T. Bender, and R. Vigneron. “The GIE S2A Full-Scale Aeroacoustic Wind Tunnel”. *SAE Technical Paper 2004-01-0808*. Mar. 8, 2004. DOI: `10.4271/2004-01-0808`.

[17] J. Sternéus, T. Walker, and T. Bender. “Upgrade of the Volvo Cars Aerodynamic Wind Tunnel”. *SAE Technical Paper 2007-01-1043*. Apr. 16, 2007. DOI: `10.4271/2007-01-1043`.

[18] A. Cogotti. “The New Moving Ground System of the Pininfarina Wind Tunnel”. *SAE Technical Paper 2007-01-1044*. Apr. 16, 2007. DOI: `10.4271/2007-01-1044`.

[19] E. G. Duell, A. Kharazi, S. Muller, W. Ebeling, and E. Mercker. “The BMW AVZ Wind Tunnel Center”. *SAE Technical Paper 2010-01-0118*. Apr. 12, 2010. DOI: `10.4271/2010-01-0118`.

[20] T. Bender, P. Hoff, and R. Kleemann. “The New BMW Climatic Testing Complex - The Energy and Environment Test Centre”. *SAE Technical Paper 2011-01-0167*. Apr. 12, 2011. DOI: `10.4271/2011-01-0167`.

[21] H. Stumpf, P. Röser, T. Wiegand, B. Pfäfflin, J. Ocker, R. Müller, W. Eckert, and H.-U. Kroß. “The new aerodynamic and aeroacoustic wind tunnel of the Porsche AG”. *15. Internationales Stuttgarter Symposium*. Wiesbaden: Springer Vieweg, 2015, pp. 811–826. DOI: `10.1007/978-3-658-08844-6_54`.

[22] F. Wittmeier, A. Michelbach, J. Wiedemann, and V. Senft. “The New Interchangeable Three-belt System in the IVK Full-Scale Wind Tunnel of University of Stuttgart: Design and First Results”. *SAE Technical Paper 2016-01-1581*. Apr. 5, 2016. DOI: `10.4271/2016-01-1581`.

[23] K. Cooper. “Bluff-body blockage corrections in closed-and open-test-section wind tunnels”. *Wind Tunnel Wall Correction (AGARD-AG-336)*. Neuilly-sur-Seine Cedex: North Atlantic Treaty Organization, 1998. ISBN: 92-836-1076-8.

[24] J. B. Barlow, A. Pope, and W. H. Rae. *Low-speed wind tunnel testing*. 3. ed. New York: Wiley, 1999. 713 pp. ISBN: 978-0-471-55774-6.

[25] R. C. Pankhurst and D. W. Holder. *Wind-tunnel technique: an account of experimental methods in low-and high-speed wind tunnels*. London: Sir Isaac Pitman & Sons, LTD., 1952. 702 pp.

[26] P. M. Waudby-Smith and W. J. Rainbird. “Some Principles of Automotive Aerodynamic Testing in Wind Tunnels with Examples from Slotted Wall Test Section Facilities”. *SAE Technical Paper 850284*. Feb. 1, 1985. DOI: `10.4271/850284`.

[27] H. C. Garner, E. W. Rogers, W. E. Acum, and E. C. Maskell. *Subsonic wind tunnel wall corrections*. AGARDograph 109. Paris: North Atlantic Treaty Organization, Oct. 1966.

[28] R. G. J. Flay, G. M. Elfstrom, and P. J. F. Clark. “Slotted-Wall Test Section for Automotive Aerodynamic Tests at Yaw”. *SAE Technical Paper 830302*. Feb. 1, 1983. DOI: `10.4271/830302`.

[29] S. Raimondo and P. Clark. “Slotted wall test section for automotive aerodynamic test facilities”. *12th Aerodynamic Testing Conference.* American Institute of Aeronautics and Astronautics, 1982. DOI: `10.2514/6.1982-585`.

[30] M. Eng. “Investigation of Aerodynamic Correction Methods Applied to a Slotted Wall Wind Tunnel”. Masters Thesis. Technische Universität Berlin, Mar. 23, 2009.

[31] E. Mercker and J. Wiedemann. “On the Correction of Interference Effects in Open Jet Wind Tunnels”. *SAE Technical Paper 960671.* Feb. 1, 1996. DOI: `10.4271/960671`.

[32] G. Wickern. “A Theoretical Approach towards the Self-Correcting Open Jet Wind Tunnel”. *SAE Technical Paper 2014-01-0579.* Apr. 1, 2014. DOI: `10.4271/2014-01-0579`.

[33] W.-H. Hucho, ed. *Aerodynamics of road vehicles: from fluid mechanics to vehicle engineering.* 4. ed. Warrendale, Pa: Society of Automotive Engineers, 1998. 918 pp. ISBN: 978-0-7680-0029-0.

[34] D. Sims-Williams. “Cross Winds and Transients: Reality, Simulation and Effects”. *SAE International Journal of Passenger Cars - Mechanical Systems* 4.1 (Apr. 12, 2011), pp. 172–183. ISSN: 1946-4002. DOI: `10.4271/2011-01-0172`.

[35] A. Cogotti. “Generation of a Controlled Level of Turbulence in the Pininfarina Wind Tunnel for the Measurement of Unsteady Aerodynamics and Aeroacoustics”. *SAE Technical Paper 2003-01-0430.* Mar. 3, 2003. DOI: `10.4271/2003-01-0430`.

[36] B. R. McAuliffe and A. D’Auteuil. “A System for Simulating Road-Representative Atmospheric Turbulence for Ground Vehicles in a Large Wind Tunnel”. *SAE International Journal of Passenger Cars - Mechanical Systems* 9.2 (Apr. 5, 2016), pp. 817–830. ISSN: 1946-4002. DOI: `10.4271/2016-01-1624`.

[37] O. Mankowski, D. Sims-Williams, and R. Dominy. “A Wind Tunnel Simulation Facility for On-Road Transients”. *SAE International Journal of Passenger Cars - Mechanical Systems* 7.3 (Apr. 1, 2014), pp. 1087–1095. ISSN: 1946-4002. DOI: `10.4271/2014-01-0587`.

[38] R. Blumrich, N. Widdecke, J. Wiedemann, A. Michelbach, F. Wittmeier, and O. Beland. “New FKFS Technology at the Full-Scale Aeroacoustic Wind Tunnel of University of Stuttgart”. *SAE International Journal of Passenger Cars - Mechanical Systems* 8.1 (Apr. 14, 2015), pp. 294–305. ISSN: 1946-4002. DOI: `10.4271/2015-01-1557`.

[39] T. Yamashita, T. Makihara, K. Maeda, and K. Tadakuma. “Unsteady Aerodynamic Response of a Vehicle by Natural Wind Generator of a Full-Scale Wind Tunnel”. *SAE International Journal of Passenger Cars - Mechanical Systems* 10.1 (Mar. 28, 2017), pp. 358–368. ISSN: 1946-4002. DOI: `10.4271/2017-01-1549`.

[40] J. Wiedemann. “Some Basic Investigations into the Principles of Ground Simulation Techniques in Automotive Wind Tunnels”. *SAE Technical Paper 890669.* Feb. 1, 1989. DOI: `10.4271/890369`.

[41] J. Wiedemann. “The Influence of Ground Simulation and Wheel Rotation on Aerodynamic Drag Optimization - Potential for Reducing Fuel Consumption”. *SAE Technical Paper 960672.* Feb. 1, 1996. DOI: `10.4271/960672`.

[42] L. Larsson, L. Hammar, L. U. Nilsson, A. Berndtsson, K. Knutson, and H. Danielson. “A Study of Ground Simulation-Correlation between Wind-Tunnel and Water-Basin Tests of a Full-Scale Car”. *SAE Technical Paper 890368.* Feb. 1, 1989. DOI: `10.4271/890368`.

[43] A. Klemin. “A Belt Method of Representing the Ground”. *Journal of the Aeronautical Sciences* 1.4 (1934), pp. 198–199. DOI: `10.2514/8.51`.

[44] A. Cogotti. “Ground Effect Simulation for Full-Scale Cars in the Pininfarina Wind Tunnel”. *SAE Technical Paper 950996.* Feb. 1, 1995. DOI: `10.4271/950996`.

[45] A. Hennig, N. Widdecke, T. Kuthada, and J. Wiedemann. “Numerical Comparison of Rolling Road Systems”. *SAE International Journal of Engines* 4.2 (June 9, 2011), pp. 2659–2670. ISSN: 1946-3944. DOI: `10.4271/2011-37-0017`.

[46] E. Mercker and J. Wiedemann. “Comparison of Different Ground Simulation Techniques for Use in Automotive Wind Tunnels”. *SAE Technical Paper 900321.* Feb. 1, 1990. DOI: `10.4271/900321`.

[47] G. Wickern, S. Dietz, and L. Luehrmann. “Gradient Effects on Drag Due to Boundary-Layer Suction in Automotive Wind Tunnels”. *SAE Technical Paper 2003-01-0655.* Mar. 3, 2003. DOI: `10.4271/2003-01-0655`.

[48] E. Mercker and H. Knape. “Ground Simulation with Moving Belt and Tangential Blowing for Full-scale Automotive Testing in a wind Tunnel”. *SAE Technical Paper 890367.* Feb. 1, 1989. DOI: `10.4271/890367`.

[49] T. Bender. *Commissioning Report: PVT Ground Simulation Upgrade.* Internal Report 4147R269. Aiolos Engineering Corporation, Dec. 21, 2006.

[50] L.-U. Nilsson and A. Berndtsson. “The New Volvo Multipurpose Automotive Wind Tunnel”. *SAE Technical Paper 870249.* Feb. 1, 1987. DOI: `10.4271/870249`.

[51] *Aerodynamics Commissioning Report Phase I Programme.* Internal Report 4034/R184. DSMA International Inc., Nov. 1986.

[52] O. Fischer, T. Kuthada, N. Widdecke, and J. Wiedemann. “CFD Investigations of Wind Tunnel Interference Effects”. *SAE Technical Paper 2007-01-1045.* Apr. 16, 2007. DOI: `10.4271/2007-01-1045`.

[53] O. Fischer, T. Kuthada, J. Wiedemann, P. Dethioux, R. Mann, and B. Duncan. “CFD Validation Study for a Sedan Scale Model in an Open Jet Wind Tunnel”. *SAE Technical Paper 2008-01-0325.* Apr. 14, 2008. DOI: `10.4271/2008-01-0325`.

[54] O. Fischer, T. Kuthada, E. Mercker, J. Wiedemann, and B. Duncan. “CFD Approach to Evaluate Wind-Tunnel and Model Setup Effects on Aerodynamic Drag and Lift for Detailed Vehicles”. *SAE Technical Paper 2010-01-0760.* Apr. 12, 2010. DOI: `10.4271/2010-01-0760`.

[55] S. Cyr, K.-D. Ih, and S.-H. Park. “Accurate Reproduction of Wind-Tunnel Results with CFD”. *SAE Technical Paper 2011-01-0158.* Apr. 12, 2011. DOI: `10.4271/2011-01-0158`.

[56] C. Collin, S. Mack, T. Indinger, and J. Mueller. “A Numerical and Experimental Evaluation of Open Jet Wind Tunnel Interferences using the DrivAer Reference Model”. *SAE International Journal of Passenger Cars - Mechanical Systems* 9.2 (Apr. 5, 2016). ISSN: 1946-4002. DOI: `10.4271/2016-01-1597`.

[57] K. Horrigan, B. Duncan, P. Sivakumar, A. Gupta, and A. Wong. “Aerodynamic Simulations of a Class 8 Heavy Truck: Comparison to Wind Tunnel Results and Investigation of Blockage Influences”. *SAE Technical Paper 2007-01-4295*. Oct. 30, 2007. DOI: `10.4271/2007-01-4295`.

[58] M. Heinecke, J. Beedy, K. Horrigan, and R. Sengupta. “Aerodynamic Study of a Production Tractor Trailer Combination using Simulation and Wind Tunnel Methods”. *SAE Technical Paper 2010-01-2040*. Oct. 5, 2010. DOI: `10.4271/2010-01-2040`.

[59] S. Perzon. “On Blockage Effects in Wind Tunnels – A CFD Study”. *SAE Technical Paper 2001-01-0705*. Mar. 5, 2001. DOI: `10.4271/2001-01-0705`.

[60] M. Olander. “CFD Simulation of the Volvo Cars Slotted Walls Wind Tunnel”. Masters Thesis. Chalmers University of Technology, 2011.

[61] A. Wall. “Simulating the Volvo Cars Aerodynamic Wind Tunnel with CFD”. Masters Thesis. Chalmers University of Technology, 2013.

[62] *Recommended Practice: Calibration of Subsonic and Transonic Wind Tunnels (AIAA R-093-2003)*. AIAA Standards. Reston, VA: American Institute of Aeronautics and Astronautics, Inc., Jan. 1, 2003. 146 pp. ISBN: 978-1-56347-661-7. DOI: `10.2514/4.476624`.

[63] *Trimble S7 Total Station Datasheet*. 2015.

[64] BIPM, IEC, IFCC, ILAC, IUPAP, ISO, OIML, and IUPAC. *Evaluation of measurement data - Guide to the Expression of Uncertainty in Measurement. JCGM 100: 2008*. Sept. 2008.

[65] M. Giordano. “Uncertainty propagation with functionally correlated quantities”. *arXiv:1610.08716 [physics]* (Oct. 27, 2016). arXiv: `1610.08716`.

[66] J. Bezanson, A. Edelman, S. Karpinski, and V. Shah. “Julia: A Fresh Approach to Numerical Computing”. *SIAM Review* 59.1 (Jan. 1, 2017), pp. 65–98. ISSN: 0036-1445. DOI: `10.1137/141000671`.

[67] C. M. Wittenbrink, A. T. Pang, and S. K. Lodha. “Glyphs for visualizing uncertainty in vector fields”. *IEEE Transactions on Visualization and Computer Graphics* 2.3 (Sept. 1996), pp. 266–279. ISSN: 1077-2626. DOI: `10.1109/2945.537309`.

[68] M. L. Shur, P. R. Spalart, M. K. Strelets, and A. K. Travin. “A hybrid RANS-LES approach with delayed-DES and wall-modelled LES capabilities”. *International Journal of Heat and Fluid Flow* 29.6 (Dec. 2008), pp. 1638–1649. ISSN: 0142-727X. DOI: `10.1016/j.ijheatfluidflow.2008.07.001`.

[69] G. E. P. Box, J. S. Hunter, and W. G. Hunter. *Statistics for Experimenters: Design, Innovation and Discovery*. 2. ed. Wiley series in probability and statistics. Hoboken, N.J: Wiley-Interscience, 2005. 633 pp. ISBN: 978-0-471-71813-0.

[70] T. Hobeika and S. Sebben. “Tyre Pattern Features and Their Effects on Passenger Vehicle Drag”. *SAE International Journal of Passenger Cars - Mechanical Systems* 11.5 (Apr. 3, 2018), pp. 401–413. ISSN: 1946-4002. DOI: `10.4271/2018-01-0710`.

[71] T. Hobeika. “Wheel Modelling and Cooling Flow Effects on Car Aerodynamics”. Doctoral thesis. Chalmers University of Technology, 2018.

[72] S. Bonitz. “Development of Separation Phenomena on a Passenger Car”. Doctoral thesis. Chalmers University of Technology, 2018.

[73] P. Ekman, T. Larsson, T. Virdung, and M. Karlsson. “Accuracy and Speed for Scale-Resolving Simulations of the DrivAer Reference Model”. *SAE Technical Paper 2019-01-0639*. Apr. 2, 2019. DOI: `10.4271/2019-01-0639`.

[74] L. Davidson. “Large Eddy Simulations: How to evaluate resolution”. *International Journal of Heat and Fluid Flow*. The 3rd International Conference on Heat Transfer and Fluid Flow in Microscale 30.5 (Oct. 1, 2009), pp. 1016–1025. ISSN: 0142-727X. DOI: `10.1016/j.ijheatfluidflow.2009.06.006`.

[75] T. Hobeika, L. Löfdahl, and S. Sebben. “Study of different tyre simulation methods and effects on passenger car aerodynamics”. *Proceedings of the IMECHE International Vehicle Aerodynamics Conference*. 2014, pp. 187–195.

[76] T. Hobeika and S. Sebben. “CFD investigation on wheel rotation modelling”. *Journal of Wind Engineering and Industrial Aerodynamics* 174 (Mar. 1, 2018), pp. 241–251. ISSN: 0167-6105. DOI: `10.1016/j.jweia.2018.01.005`.

[77] S. Koitrand, A. Gaylard, and G. O. Fiet. “An Investigation of Wheel Aerodynamic Effects for a Saloon Car”. *Progress in Vehicle Aerodynamics and Thermal Management: Proceedings of the 10th FKFS-Conference*. Renningen: Expert-Verlag, 2015. ISBN: 978-3-8169-3322-9.

[78] G. Wickern and E. Beese. “Computational and Experimental Evaluation of a Pad Correction for a Wind Tunnel Balance Equipped for Rotating Wheels”. *SAE Technical Paper 2002-01-0532*. Mar. 4, 2002. DOI: `10.4271/2002-01-0532`.